Journal of Electronic Materials
https://doi.org/10.1007/s11664-023-10526-3

ORIGINAL RESEARCH ARTICLE

Tuning the Properties of Reduced Graphene Oxide-$Sr_{0.7}Sm_{0.3}Fe_{0.4}Co_{0.6}O_3$ Nanocomposites as Potential Photoanodes for Dye-Sensitized Solar Cells

Samantha Ndlovu[1] · Edigar Muchuweni[2] · Moses A. Ollengo[1] · Vincent O. Nyamori[1]

Received: 5 December 2022 / Accepted: 22 May 2023

Abstract

The generation of electricity using solar energy is an effective system to overcome the current global energy crisis. In this regard, developing new semiconductor materials can be of great interest in overcoming the challenge of charge carrier recombination and, hence, improving the power conversion efficiency (PCE) in photovoltaic devices, particularly dye-sensitized solar cells (DSSCs). Here, reduced graphene oxide-$Sr_{0.7}Sm_{0.3}Fe_{0.6}Co_{0.4}O_3$ (RGO-SSFC) nanocomposites were synthesized using the hydrothermal method and characterized with the aid of microscopic and spectroscopic techniques, as well as a vibrating sample magnetometer, and further tested for application as photoanodes in DSSCs. Scanning electron microscopy revealed the presence of RGO nanosheets that were fully decorated by irregular- and spherical-shaped SSFC nanoparticles. Fourier-transform infrared spectroscopy confirmed the strong synergistic interaction of the RGO-SSFC nanocomposites. The large surface area of RGO-SSFC nanocomposite photoanodes facilitated effective dye loading, high photon absorption, and efficient electron transfer, resulting in better device performance. Compared to RGO-SSFC-0.1 and RGO-SSFC-1.0, the RGO-SSFC-0.5 nanocomposite showed an enhanced open-circuit voltage (V_{oc}) of 0.84 V, short-circuit current density (J_{sc}) of 14.02 mA cm^{-2} , and a PCE of 7.25%. Eosin B and MK-2 organic dyes used as photosensitizers coated on the RGO-SSFC semiconductors resulted in low-cost DSSC photoanodes.

Graphical Abstract

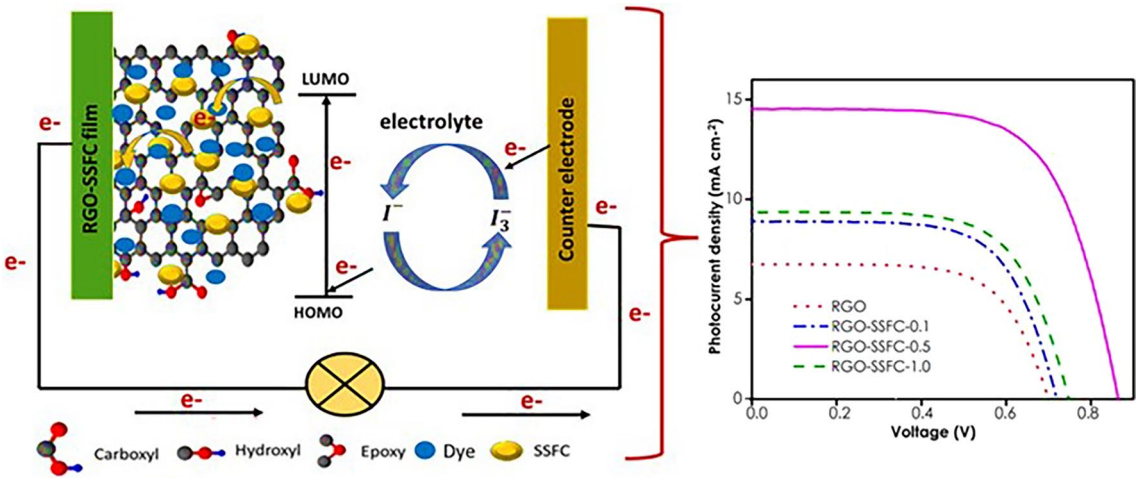

Keywords Dye-sensitized solar cell · graphene · nanocomposites · organic dyes · perovskite oxides · semiconductors

Extended author information available on the last page of the article

Published online: 04 July 2023

Introduction

Different inorganic and organic semiconductors have been mainly used as solar energy harvesters in hybrid photovoltaics (PVs) due to their low-cost, facile fabrication processes and excellent power conversion efficiency (PCE).[1–4] Dye-sensitized solar cells (DSSCs) are part of hybrid PVs with laboratory-scale devices that have reached PCEs of ~ 14.0%.[5,6] Metal oxide semiconductors, such as titanium dioxide (TiO_2) and zinc oxide (ZnO), have been mostly used as photoanode materials in DSSCs due to their excellent charge carrier transport properties.[7–10] However, these semiconductors have wide band gaps, which lead to poor charge carrier transportation and high charge carrier recombination, resulting in low PCE.[11] To mitigate these issues, carbon-based materials, such as carbon nanotubes and graphene-based materials, have been introduced as alternatives or additives to TiO_2[12] and ZnO[13] to assist in transporting electrons to the transparent conducting electrode. However, carbon-based DSSCs still exhibit relatively low PCE due to ultra-fast charge carrier recombination and restacking of the graphene sheets.[14] Therefore, developing novel semiconductor nanocomposites with improved charge separation and low charge carrier recombination can be a better option.

Graphene can be easily modified as an electron acceptor to form a low band gap that is suitable for optoelectronic applications.[15] Graphene-based materials have shown remarkable properties, such as high charge carrier mobility,[16] enhanced surface area,[17] suitable chemical properties,[18] high optical transmittance in the visible region, and high electrical conductivity.[19,20] Graphene and its derivatives can be synthesized using chemical functionalization, i.e., covalent or non-covalent interactions, to form different graphene-based materials with unique oxidation levels.[21,22] Functionalization normally leads to the disruption of the carbon sp^2 lattice, which can change the physical, chemical, and electronic properties, and, thus, enhance the electrical conductivity and free charge densities.[16] Graphene derivatives, particularly graphene oxide (GO), can be prepared using various starting materials, such as polymers,[23,24] biomass waste,[25] or natural graphite.[26] GO sheets can be highly oxidized and characterized by their main functional groups, such as alcohol, carboxylic acid, and epoxides.[27] The presence of oxygenated functional groups on GO makes the material hydrophilic in nature, thus allowing it to be easily dispersed in water. It is also easy to chemically functionalize GO to form a semi-metallic state of reduced graphene oxide (RGO).[28] The remaining oxygen functional groups on RGO can be used as an advantage to facilitate the interaction with polymer or metal oxides.[29] RGO can be used to support most nanoparticles since it has outstanding electrical conductivity, high specific surface area, and tremendous chemical stability.[30]

On the other hand, perovskite-type oxides with the chemical form (ABO_3) have attracted scientists' attention due to their magnetic, electrical, and optical properties.[31,32] Within ABO_3, the A-site is formed by a rare-earth or an alkali-earth metal ion, and any transition metal ion can form the B-site. In contrast, the oxygen stoichiometry can be changed, and combining the three sites results in unusual physical properties.[31] In particular, ferrite perovskite oxides are stimulating materials mainly because of their unique features, such as ideal band gaps[33] and controllable particle sizes.[34] The presence of iron can strongly influence the perovskite material to absorb light in the visible region.[35] Researchers have focused on finding perovskite oxides that are chemically stable, less expensive, and with good catalytic properties.[36–38] Xie et al.[39] demonstrated the use of orthorhombic $Sm_{1-x}Sr_xFe_{0.7}Co_{0.3}O_3$ as a cathode in solid oxide fuel cells. They observed an enhancement in the electrical conductivity and thermal expansion coefficient upon increasing the content of Sm^{3+}. Chima et al.[36] prepared $Sm_{0.8}Sr_{0.2}Fe_{1-x}Co_xO_3$ with smaller crystallite sizes which improved the electrocatalytic activity, demonstrating the suitability of $Sm_{0.8}Sr_{0.2}Fe_{1-x}Co_xO_3$ for use in the oxygen evolution reaction.

There is still a gap in developing graphene-based materials combined with complex perovskite oxides to form a novel nanocomposite that can possess multipurpose solar cell properties. Not much has been explored on the preparation of reduced graphene oxide-$Sr_{0.7}Sm_{0.3}Fe_{0.4}Co_{0.6}O_3$ (RGO-SSFC) nanocomposites using hydrothermal synthesis. Here, we report the synthesis of semiconductor materials of SSFC that combine with RGO to form RGO-SSFC nanocomposites as photoanodes in a DSSC system. The study of RGO-SSFC nanocomposites can be of great interest to obtain exceptional properties that can be employed as semiconductors in DSSCs. This can be done by forming a strong synergistic interaction between RGO and SSFC nanoparticles to create more enhanced optical and electrical properties suitable for application as semiconductors in photoanodes.[40] For comparison purposes, two dyes, Eosin B and MK-2, were applied as light harvesters to investigate if a change of the light harvester can be influenced by various synthesized RGO-SSFC nanocomposites.

Material and Methods

Materials

Strontium(II) acetylacetonate (97%), iron(III) acetylacetonate (97%), samarium(III) acetylacetonate hydrate (99%),

cobalt(III) acetylacetonate hydrate (97%), sulfuric acid (98%), hydrogen peroxide (100%), potassium permanganate (99.32%), guanidinium thiocyanate (99%), 1-methyl-3-propylimidazolium iodide (98%), lithium iodide (99.9%), 4-tert-butylpyridine (96%), poly(vinyl acetate) (99.9%), acetonitrile (≥ 99.9%), Eosin B (97%), MK-2 dye (95%), indium tin oxide (ITO) (15 Ω/sq, 30 × 30 × 0.7 mm), and graphite powder (99.9%) were purchased from Sigma-Aldrich, and no further purification was carried out on the commercial metal acetylacetonates.

Preparation of SSFC

A well-mixed metal acetylacetonate powder (2 g) was transferred into a 250-mL stainless jar containing stainless-steel balls, with the ball to mass ratio of 8:1. It was ball-milled using a high-energy planetary ball mill (PM 400 MA; Retsch), with eight balls for 5 h at 300 rpm, under air atmosphere. The obtained powder was calcined using a Sentro Tech furnace at 600 °C for 10 h to form the perovskite oxide product.

Preparation of GO

GO was prepared by means of oxidation and exfoliation from natural graphite using the modified Hummers' method.[29,41] Briefly, graphite powder (5 g) was added to a mixture of sodium nitrate (2.5 g) and concentrated sulfuric acid (115 mL) in a 1000-mL round-bottom flask while being stirred in an ice bath (0 °C). Potassium permanganate (15 g) was slowly added in small doses to allow the reaction mixture to remain below 5 °C to avoid excessive heat and to prevent an explosion. The reaction was heated at 35 °C with stirring for 3 h and further treated with 300 mL of 3% hydrogen peroxide to produce a pronounced exothermal effect at 98 °C, with further stirring for 30 min. The reaction mixture was continuously washed with double-distilled water to completely remove the acidity and to neutralize the pH to 7. The product was washed and centrifuged using distilled water and ethanol, and then dried in an oven overnight at 70 °C.

Preparation of RGO and RGO-SSFC Nanocomposites

The RGO-SSFC nanocomposites were synthesized using a hydrothermal reaction. Typically, in the synthesis, GO (1.00 g) in 50 mL of absolute ethanol solution (reducing agent) was sonicated for 1 h to form a homogeneous suspension. Then, 0.1 wt.% of SSFC (0.001 g) was mixed with the suspension and stirred for another 30 min. The resulting black colloidal suspension was then added to a Teflon-lined stainless-steel autoclave and kept inside the oven at 160 °C for 10 h, after which the product was centrifuged with ethanol and double-distilled water. The SSFC nanoparticles anchored on the RGO nanosheets were dried overnight in a vacuum oven at 50 °C. The SSFC concentration was varied (0.1 wt.%, 0.5 wt.%, or 1.0 wt.%) on each synthesis. For RGO preparation, a similar method was carried out with no addition of SSFC. All the materials were further characterized using different techniques.

Light-harvesting Experiments

The RGO-SSFC nanocomposite (50 mg) was mixed with absolute ethanol (0.15 mL), as reported elsewhere.[42] The mixture was sonicated in an ultrasonic water bath for 30 min. Then, the dispersed mixture was deposited onto ITO-coated glass through the doctor blade method.[43] The coated photoanode was annealed at 80 °C for 20 min using a hot plate. The film thickness (0.07 mm) was controlled using Scotch tape, which was placed on the end sides of the ITO substrate to prevent the flow of the gel electrolyte and to leave the active area uncovered. Two separate dyes (Eosin B and MK-2) were employed as light harvesters for comparison purposes. The prepared photoanode was dipped with Eosin B (or MK-2) dye (0.3 mM). The iodine-gel electrolyte was prepared and applied as the redox material and added to the active area.[44] Aluminum was used as the counter electrode. The device was assembled using an ITO glass substrate, an anode soaked with dye, followed by the gel electrolyte, and sandwiched using an aluminum counter electrode, before 1 sun (100 mW cm^{-2}) illumination. The DSSC photoactive layer was 0.98 cm^2.

Characterization

The microstructural features of the nanocomposites were evaluated using transmission electron microscopy (TEM; JEM-2100; JEOL). The surface morphologies of the nanocomposites were determined by field-emission scanning electron microscopy (FESEM; JSM-6100; JEOL), equipped with energy-dispersive x-ray spectroscopy (EDX). The phase characteristics were investigated using a powder x-ray diffractometer (XRD; AXS D8 Advance; Bruker) with a radiation source of high-intensity Cu Kα at a wavelength of 0.154 nm. The crystallinity was studied with a Raman spectrometer (Advantage 532™; DeltaNu) at the wavelength of 515 nm, equipped with NuSpec™ software. Different thermal stabilities of the nanocomposites were measured using a using a Q600 series™ Thermal Analyzer (Hitachi) at the rate of 10 °C min^{-1} from 30 °C to 1000 °C. A Micromeritics ASAP 2010 instrument was used to measure the textural properties. A Fourier-transform infrared (FTIR) spectrometer (Spectrum 100; Perkin Elmer) was used to examine different functional groups of the materials by preparing RGO-SSFC:KBr (0.003:0.024 g) pellets.

The chemical composition of the samples was examined using an elemental analyzer (Analysensysteme; Elementar). The ultraviolet–visible (UV–Vis) absorption spectra used for absorbance were determined using a spectrophotometer (UV–Vis NIR; Shimadzu). Photoluminescence (PL) emission spectra for charge recombination analysis were analyzed using a fluorescence spectrometer (LS35; Perkin Elmer) at an excitation at 300 nm, excitation slit at 5 nm, spectrum range of 580–750 nm, and scan speed of 120 nm $min^{-1;}$. A 7404 vibrating sample magnetometer was used to study the magnetic properties of the nanocomposites. A four-point probe source meter (2400 Keithley) was used to measure the electrical conductivity of the various SSFC, RGO, and RGO-SSFC. Cyclic voltammetry (CV) and electrochemical impedance spectroscopy (EIS) were measured using an electrochemical workstation (797 VA Compitrane; Metrohm) in the potential range of − 0.6 V to 0.4 V at the scan rate of 100 mV s^{-1}. The counter electrode, reference electrode, electrolyte, and working electrode were Pt, Ag/AgCl, KOH (3 M), and the prepared samples, respectively. The prepared samples were mixed with Nafion binder in the presence of absolute ethanol and sonicated for 10 min and then cast as the working electrode. The photovoltaic parameters were determined using a solar simulator (Keithley). The solar simulator lamp was a short AKC 150-W (Xenon), the air mass was 1.5 G, the frequency was 50–60 Hz, and the voltage was 116–220 V, with a maximum power of 750 W.

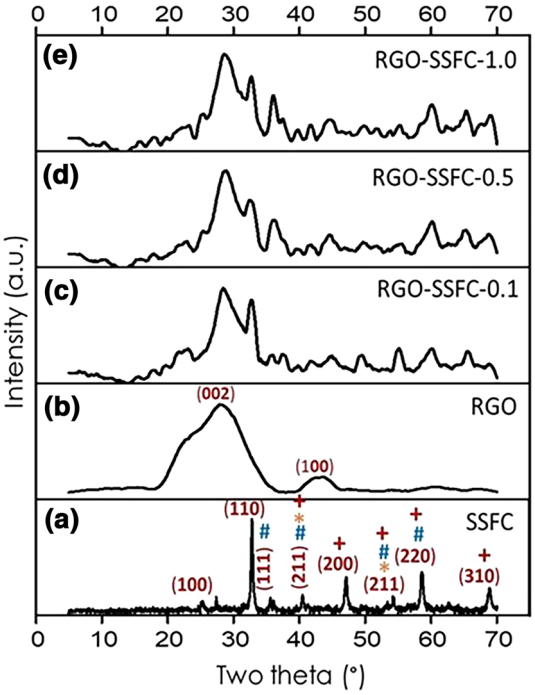

Fig. 1 X-ray diffractograms of (a) SSFC, (b) RGO, (c) RGO-SSFC-0.1, (d) RGO-SSFC-0.5, and (e) RGO-SSFC-1.0. The symbols #, + and * denote $Sr(Co_{0.81}Fe_{0.19})_{2.78,}$ $SrCoO_{2.80}$, and Fe_2O_3 phase structures, respectively.

Results and Discussion

Phase Composition

Powder XRD was used to identify the crystalline phases of the SSFC, RGO, RGO-SSFC 0.1 wt.% (RGO-SSFC-0.1), RGO-SSFC 0.5 wt.% (RGO-SSFC-0.5), and RGO-SSFC 1.0 wt.% (RGO-SSFC-1.0), as shown in Fig. 1. RGO was noted to have a diffraction peak at ~ 28°, corresponding to the (002) and (100) planes. Fu et al.[45] reported a similar study. The diffraction pattern of SSFC revealed the perovskite oxide structure to be cubic with the Pm3m space group. The prominent peaks of SSFC at 2θ = 25°, 32°, 35°, 41°, 48°, 54°, 59°, and 69° correspond to the (100), (110), (210), (211), (200), (211), (220), and (310) crystal planes, respectively. The sharp peak at 32° (110) illustrates the presence of SSFC, which appeared to overlap with the RGO broad peak on the nanocomposites.[46] The added concentration of SSFC onto RGO was the most sufficient for the signal to be notable. However, comparing SSFC to other peaks (RGO and RGO-SSFC) they looked smaller, which resulted in poor detection of SSFC peaks on the nanocomposite. The primary phase structures obtained were $Sr(Co_{0.81}Fe_{0.19})O_{2.78}$, $Fe_2O_{3,}$ and $SrCoO_{2.80,}$ as indicated by JCPD files, i.e., JCP2: 82–2445, JCP2: 33–0664, and JCP2: 27–1084, respectively. The presence of primary phase structures resulted in a severe decrease in the crystallinity of the nanocomposites.

The crystal stability of SSFC was calculated using the Goldschmidt tolerance factor (t), as shown in Eq. 1:

$$t = \frac{1}{\sqrt{2}}\left(\frac{r_A + r_o}{r_B + r_o}\right) \tag{1}$$

where r_A, r_B , and r_O are the ionic radii.[47] The t value of the perovskite structure generally ranges from 0.75 to 1.0. When the t value is close to 1, the perovskite oxide ideal cubic structure can be formed. The t value for SSFC has been calculated and found to be 0.95, which indicates some slight distortion in the structure. The crystallite sizes were calculated using the Scherrer equation (Eq. 2):

$$D = \frac{k\lambda}{\beta cos\theta} \tag{2}$$

where k is the shape factor (0.9), λ is the X-ray wavelength (1.541 Å), β is the full width at half-maximum, and θ is the diffraction angle. The crystallite sizes were found to be 24.3 nm, 23.6 nm, 23.9 nm, and 24.2 nm for SSFC,

RGO-SSFC-0.1, RGO-SSFC-0.5, and RGO-SSFC-1.0, respectively.

Microstructure and Morphology

TEM Analysis

The TEM images in Fig. 2a and b showed SSFC nanoparticles and exfoliated RGO sheets, respectively. Figure 2c–e reveal the RGO sheets fully decorated by SSFC nanoparticles. A similar microstructure was observed by Li et al.[48] in their $CoFe_2O_4$-functionalized graphene sheets. The average particle sizes of SSFC, RGO-SSFC-0.1, RGO-SSFC-0.5, and RGO-SSFC-1.0 were calculated to be 24.3 nm, 23.7 nm, 23.9 nm, and 24.2 nm, respectively, which would contribute positively in enhancing the electrochemical properties. These results were comparable to the crystallite size results obtained in powder XRD analysis (Sect. "Phase Composition").

SEM Analysis

SEM analysis was carried out to observe the surface morphology, whereby Fig. 3a revealed the RGO nanosheets with some wrinkles, due to the presence of some oxygen functional groups.[48] After the exfoliation and reduction of GO, the remaining oxygen and OH- groups would be useful in binding with some SSFC nanoparticles. The RGO-SSFC nanocomposites, shown in Fig. 3b–d, represent the RGO sheets decorated by SSFC nanoparticles. Hu et al. noted similar findings.[49] These results agree with our findings obtained from the TEM analysis, shown earlier in Fig. 2. The SEM image of SSFC, shown in Fig. 4a, reveals a mixture of irregular- and spherical-structured nanoparticles on the SSFC surface. In Fig. 4b, RGO-SSFC-0.1 exhibited more spherical-structured SSFC nanoparticles decorating the RGO sheet. The EDX spectrum and elemental mapping, shown in Fig. 4c and d, respectively, and Table I, indicate the presence of Sr, Sm, Co, Fe, C, and O functional groups on the nanocomposites. In the elemental mapping, the distribution of elements was noted to be varied throughout the RGO sheet.

Elemental Analysis

The elemental composition of the samples is shown in Table I. For SSFC, the elemental analysis revealed the presence of O without carbon and hydrogen. The remaining elements for SSFC, i.e., Sr, Sm, Fe and Co, were detected by EDX analysis, as shown in Fig. 4c and d. The O content of RGO was noted to significantly decrease from GO to RGO, which indicates the reduction of oxygen-containing functional groups, such as carboxyl, carbonyl, epoxide, and hydroxyl, that occur on the sp^2 carbon basal plane. This indicates that GO was successfully reduced using absolute ethanol during the hydrothermal treatment. The reduction of GO

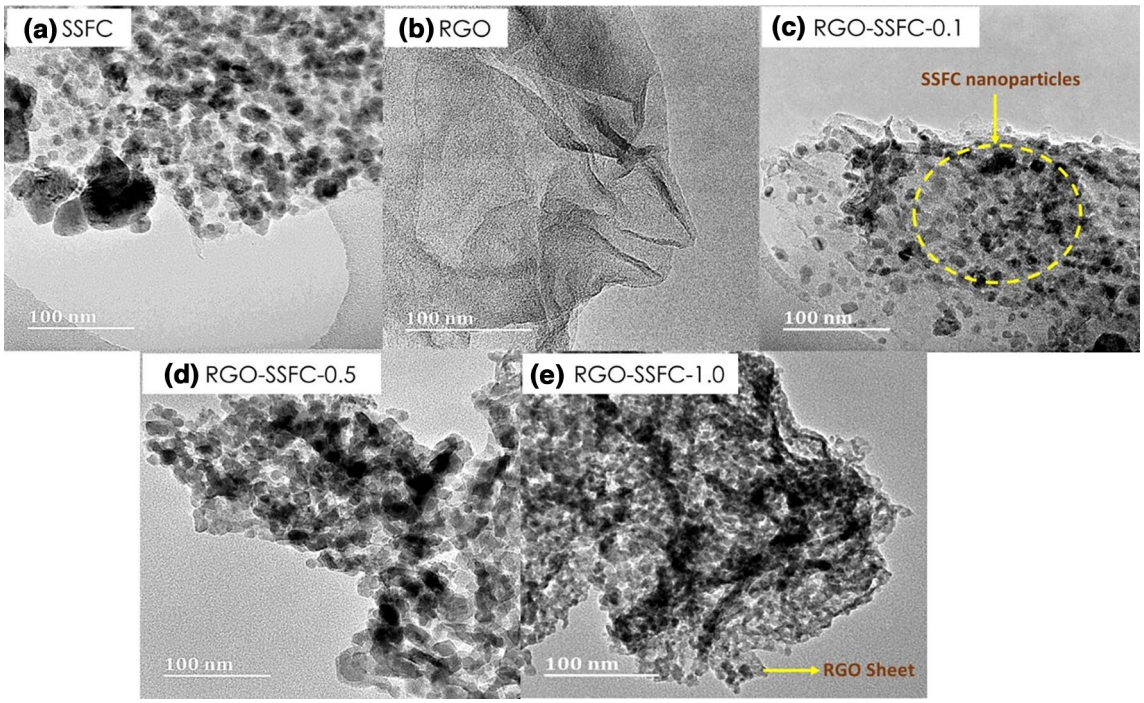

Fig. 2 TEM images of (a) SSFC, (b) RGO, (c) RGO-SSFC-0.1, (d) RGO-SSFC-0.5, and (e) RGO-SSFC-1.0.

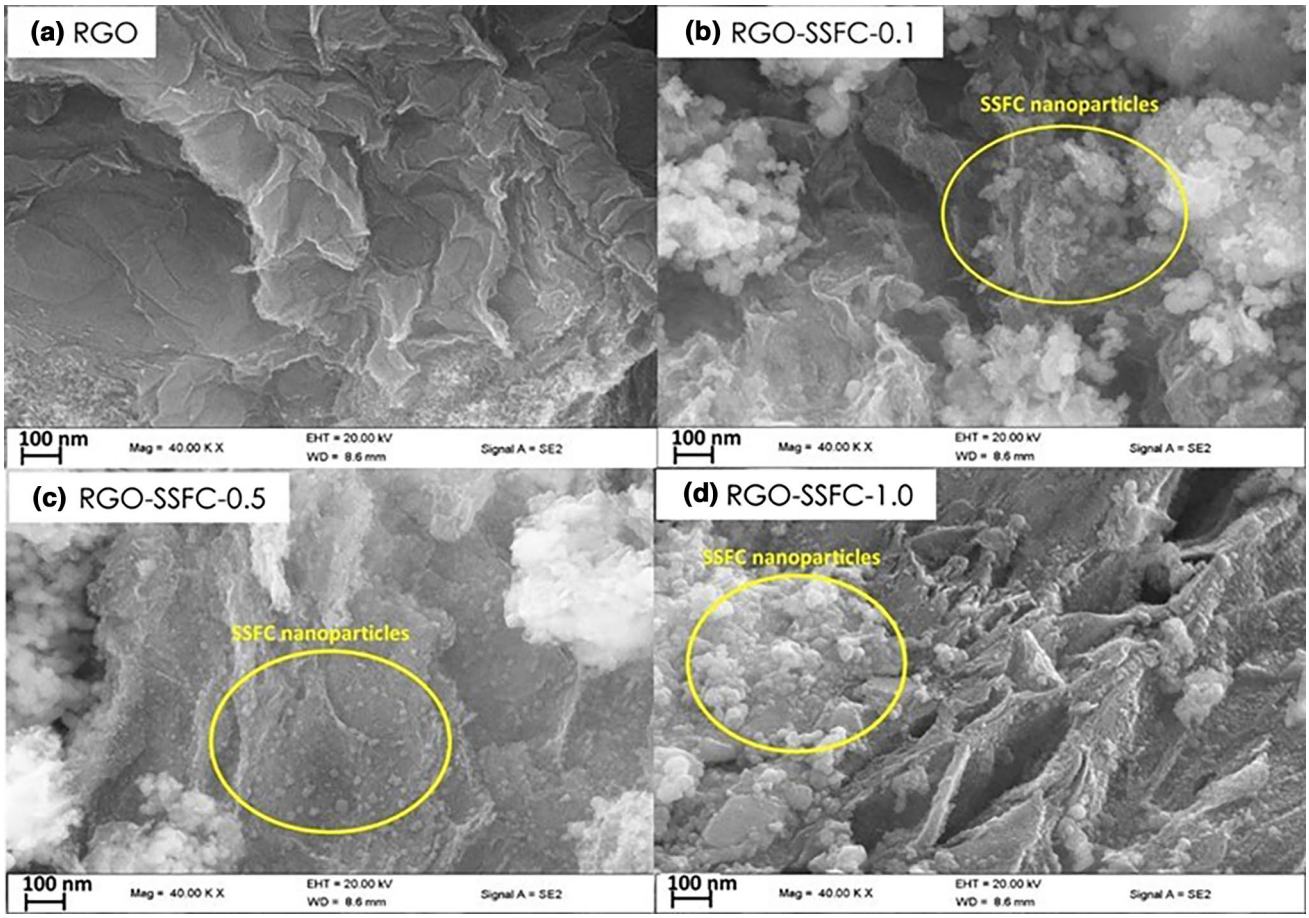

Fig. 3 SEM images of (a) RGO, (b) RGO-SSFC-0.1, (c) RGO-SSFC-0.5, and (d) RGO-SSFC-1.0.

is vital because oxygen functional groups can cause structural inhomogeneity and reduce electron mobility which would decrease the efficiency of solar cells.[50] In the nanocomposites, the C content was noted to decrease as compared to RGO because the interaction of RGO and perovskite oxide normally occurs at the $\pi - \pi$ of the C-C backbone.[51] In addition, the decrease in O as the concentration of SSFC increases can be related to the SSFC nanoparticles binding to the oxygenated functional groups of the RGO sheet. Thus, introducing a high SSFC concentration to the RGO sheets resulted in less O formed on the nanocomposites.

Structural Properties

The structural properties of the RGO-SSFC nanocomposites were studied using Raman spectra, as shown in Fig. 5. In Fig. 5a, the dominant peak of SSFC at around 700 cm^{-1} corresponds to an asymmetric stretching mode of the M-O-M bonds (M denotes the metal cations Co and Fe). This was consistent with Sithole et al.,[52] who observed similar findings of an asymmetric stretching mode of FeCo-O-FeCo bonds at ~ 700 cm^{-1}. The asymmetric stretching mode at 700 cm^{-1} was observed on all the nanocomposites, confirming that the SSFC nanoparticles were incorporated into the RGO sheets. The Raman spectra of RGO and RGO-SSFC (see Fig. 5b) exhibit two major peaks, which are typical of the D-band (between 1353 cm^{-1} and 1360 cm^{-1}) and G-band (between 1545 cm^{-1} and 1552 cm^{-1}). The D-band peak originates from the edge sp^3 defects or due to in-plane disordered carbon, whereas the G-band can be associated with the in-plane vibrations of the ordered sp^2-hybridized bonded carbon atoms.[53] A higher I_D/I_G ratio correlates with a higher degree of disorder of the sp^2-hybridized C=C RGO structure, which also reduces the graphitic nature of the RGO nanocomposites. As the amounts of SSFC were added to the nanocomposite, i.e., from RGO (without SSFC), RGO-SSFC-0.1, RGO-SSFC-0.5, to RGO-SSFC-1.0, the I_D/I_G ratios increased and were 0.82, 1.05, 1.32, and 1.50, respectively (see Supplementary Table SI). The low I_D/I_G ratio of RGO indicates that the defect decreases as the reduction process of the oxygenated functional groups partially restores the sp^2 domain. The addition of SSFC onto the RGO sheet had a higher I_D/I_G , suggesting that more defects were created due to the formation and increase in the

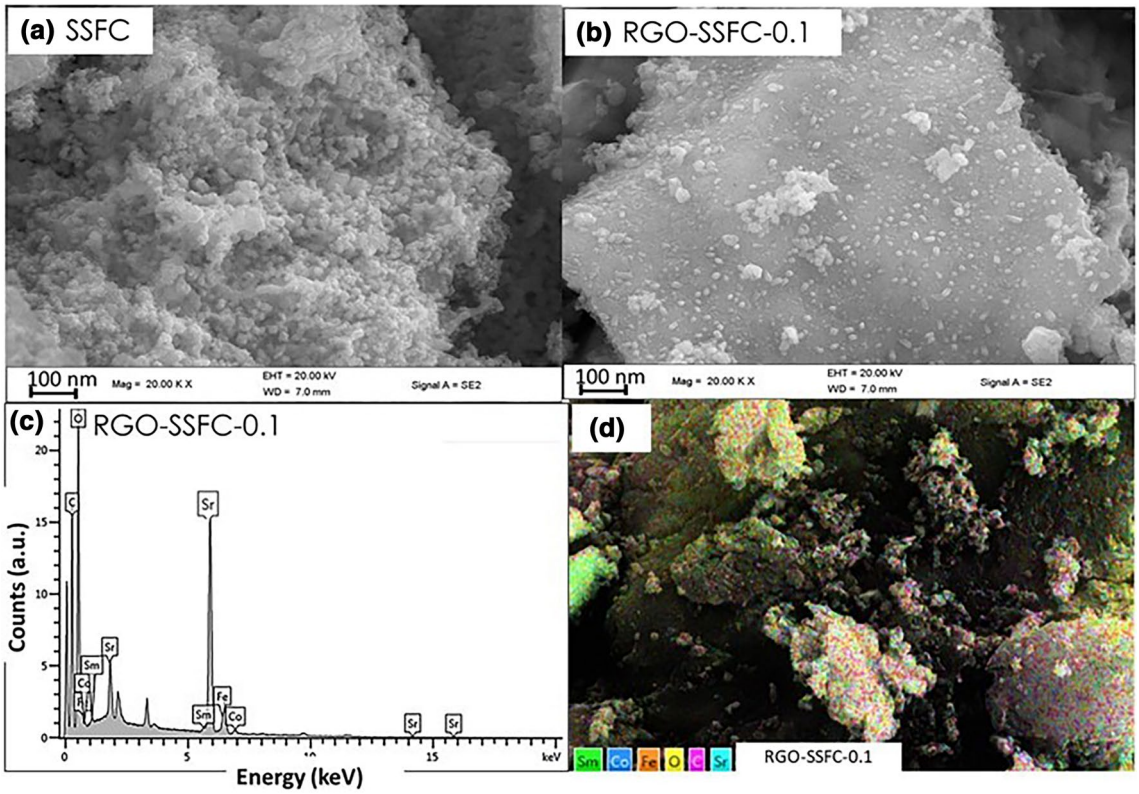

Fig. 4 SEM images of (a) SSFC, (b) RGO-SSFC-0.1, (c) EDX spectrum, and (d) elemental mapping of RGO-SSFC-0.1.

Table I Elemental and EDX analysis of the prepared materials

Samples	Elemental analysis			EDX analysis			
	Carbon (%)	Hydrogen (%)	Oxygen (%)	Strontium (%)	Samarium (%)	Iron (%)	Cobalt (%)
SSFC	–	–	24.93	31.85	22.88	11.61	8.73
GO	56.66	1.96	41.38	–	–	–	–
RGO	74.02	1.92	24.06	–	–	–	–
RGO-SSFC-0.1	45.90	1.20	15.50	15.81	11.91	5.67	4.01
RGO-SSFC-0.5	45.78	1.85	13.97	15.88	11.98	5.96	4.58
RGO-SSFC-1.0	45.98	1.81	12.86	15.98	12.49	5.97	4.91

sp^2 hybridization. Also, the I_D/I_G ratios of the RGO-SSFC nanocomposites were noted to increase with the content of SSFC, which showed the increase in structural defects upon the addition of SSFC nanoparticles onto the RGO lattice. This observation was consistent with the elemental analysis results, which revealed a decrease in oxygen atoms upon the deposition of SSFC nanoparticles onto the RGO sheets. Thus, introducing SSFC nanoparticles creates more defect sites on the RGO-SSFC nanocomposite surface, enabling the application of the nanocomposite as an electrocatalyst.[54]

Functional Groups

FTIR analysis was used to examine different functional groups of the SSFC, RGO, and RGO-SSFC nanocomposites, as illustrated in Fig. 6. In Fig. 6a, the SSFC dominant peaks can be seen observed at 480 cm^{-1}, 570 cm^{-1}, 850 cm^{-1} , and 1500 cm^{-1}, representing the metal–oxygen (M-O) of the Fe-O vibration in an octahedral environment, the Co-O vibration occupying an octahedral environment, asymmetric stretching modes of M-O-M (M denoted metal cations Fe and Co), and the O-H bond of free water in the SSFC, respectively.[52] The presence of the O-H bond was also observed in the elemental analysis, as shown in Table I.

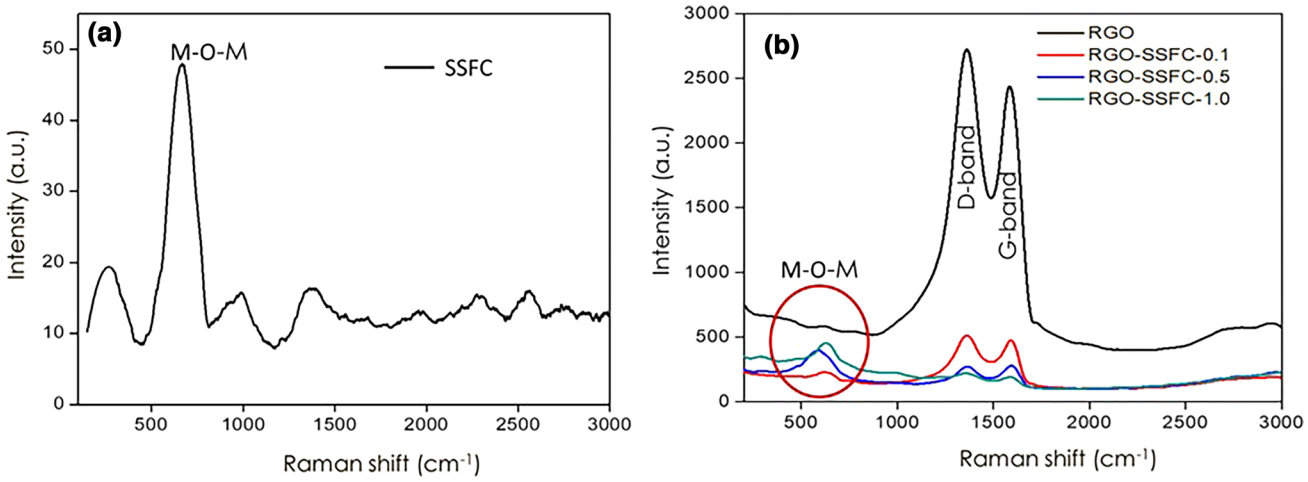

Fig. 5 Raman spectrum of (a) SSFC and (b) Raman spectra of RGO and RGO-SSFC nanocomposites; *M* denotes metal cations Fe and Co.

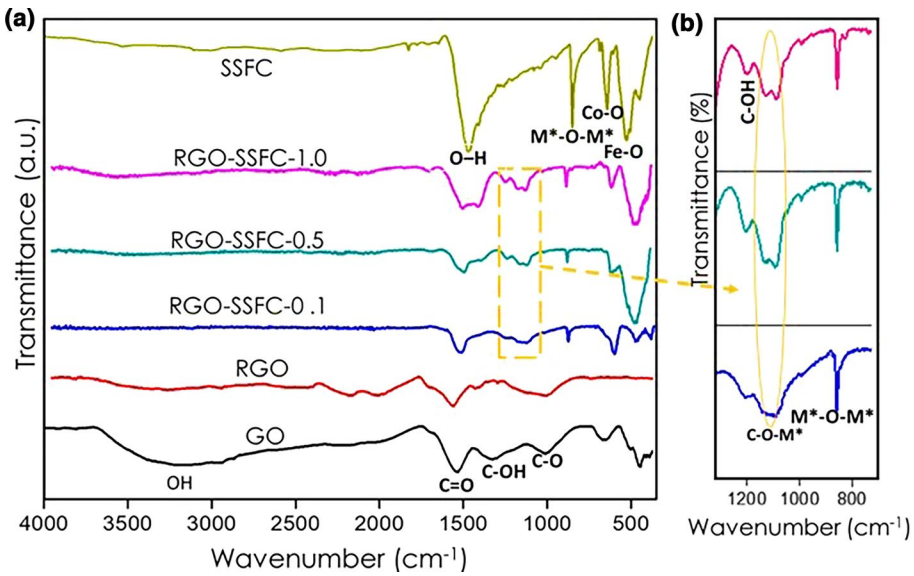

Fig. 6 FTIR spectra of (a) the overall view of all the materials and (b) a closer view of the nanocomposites. *M* denotes metal cations Fe and Co.

However, the O-H bond can be useful in binding with SSFC elements (Sr, Sm, Fe, and Co). The FTIR spectrum of GO confirms the exfoliation and reduction of GO to RGO. GO was noted to have peaks at around 1000 cm^{-1}, 1450 cm^{-1}, 1630 cm^{-1} , and 3200 cm^{-1}, which signify the C-O, C=C aromatic ring, C=O, and O-H stretching modes, respectively.[48] GO was reduced using absolute ethanol to form RGO with fewer oxygen functional groups. This is consistent with the elemental analysis results (see Table I), which revealed a decrease in oxygen content from 41.38% for GO to 24.06% for RGO. The remaining functional groups, such as oxygen on the graphene sheets attached to the edge or surface, can act as the nucleation sites of the SSFC nanoparticles.[55] The characteristic peaks of RGO at 1730 cm^{-1}, 1500 cm^{-1} , and 1000 cm^{-1} represent the functional groups of the C=O stretching band of the carbonyl, the C=C aromatic ring, and C-O, respectively.

When comparing RGO-SSFC to RGO, new sharp peaks were observed around 480 cm^{-1} due to the metal and oxygen bonds (Fe-O) stretching mode. Also, SSFC and RGO-SSFC have bands around 570 cm^{-1}, representing the Co–O bands,[56] while the bands at 850 cm^{-1} signify the M-O-M resonance. Similar findings were also observed by Raman analysis, which signifies the formation of the M-O-M peak at around 700 cm^{-1}. The formation of new peaks on the RGO-SSFC nanocomposites was observed at ~ 1100 cm^{-1}, which signifies the C-O-M bond (M symbolizes the metal ion of either Sr, Sm, Fe, or Co).[55] The peak at 1200 cm^{-1} signifies the C-OH bond. The bands at 1600 cm^{-1} represent the C=C aromatic ring on the surface of the graphene sheet. From the FTIR in Fig. 6b, we can

conclude that there was some strong synergistic interaction between RGO and SSFC due to the formation of new covalent bonds between the two materials.

Surface Area

Different surface areas and pore size distributions of RGO-SSFC were studied using the Brunauer–Emmett–Teller technique, and the results are presented in Table II. SSFC had the lowest surface area of 27 $m^2\ g^{-1}$, while RGO exhibited the highest of 105 $m^2\ g^{-1}$. The addition of SSFC onto the RGO sheet as the support significantly increased the surface area of the RGO-SSFC. The surface area increased from 27 $m^2\ g^{-1}$ for SSFC to above 85 $m^2\ g^{-1}$ for the RGO-SSFC nanocomposites. A similar trend was observed by Li et al.[57] in their $BiFeO_3$/graphene nanocomposites, which showed an increase in surface area from 21.3 $m^2\ g^{-1}$ ($BiFeO_3$) to 55.3 $m^2\ g^{-1}$ ($BiFeO_3$/graphene). The relatively lower surface area for RGO-SSFC compared to RGO was attributed to SSFC, which tended to close most of the RGO sheet pores, as revealed by TEM images in Fig. 2. The large surface area obtained for RGO-SSFC would be beneficial for effective dye loading, which subsequently leads to more light harvesting in solar cells.[58,59] All the prepared samples exhibited pore sizes below 20 nm, which belong to mesoporous materials, as reported by Ngidi et al.[60]

Table II Surface areas and porosities of RGO, SSFC, and RGO-SSFC

Samples	Surface area ($m^2\ g^{-1}$)	Pore volume ($cm^3\ g^{-1}$)	Pore size (nm)
SSFC	27	0.197	13.02
RGO	105	0.230	1.80
RGO-SSFC-0.1	91	0.298	4.50
RGO-SSFC- 0.5	96	0.291	4.20
RGO-SSFC-1.0	85	0.275	4.24

The nitrogen adsorption–desorption isotherms of the samples are shown in Supplementary Fig. S1. SSFC, in Supplementary Fig. S1a, exhibited type IV adsorption–desorption isotherms with the H1 hysteresis loop in the range from 0.8 P/P_o to 1.0 P/P_o , having regular spherical-shaped pores, which have the advantage of increasing the surface area of adsorption and desorption of the ions. RGO and RGO-SSFC, in Supplementary Fig. S1(b-e), also exhibited type IV adsorption–desorption isotherms but with H3-type hysteresis loops, having plate-like particles in the range from 0.55 P/P_o to 1.0 P/P_o.[61] Compared to SSFC, RGO reveals a larger hysteresis loop due to the formation of a larger surface area. Interestingly, the addition of RGO onto SSFC increased the surface area of the RGO-SSFC nanocomposites, which is beneficial for improving the insertion and de-insertion of ions during the charging and discharging processes, resulting in enhanced electrochemical properties.

Thermal Stability

The decomposition behavior of the various prepared samples was analyzed using thermogravimetric (TGA) analysis, shown in Fig. 7. All the samples exhibited weight losses between 0 °C and 150 °C due to water or adsorbed moisture removal. The decomposition of the oxygenated functional groups (carbonyl, epoxide, and hydroxyl), amorphous carbon groups, and CO_x species (carbon dioxide and carbon monoxide) was observed between 200 °C and 400 °C.[62]

When comparing RGO to RGO-SSFC, RGO was noted to be more thermally stable with a decomposition temperature of 500 °C and residual content of 9%. However, with the

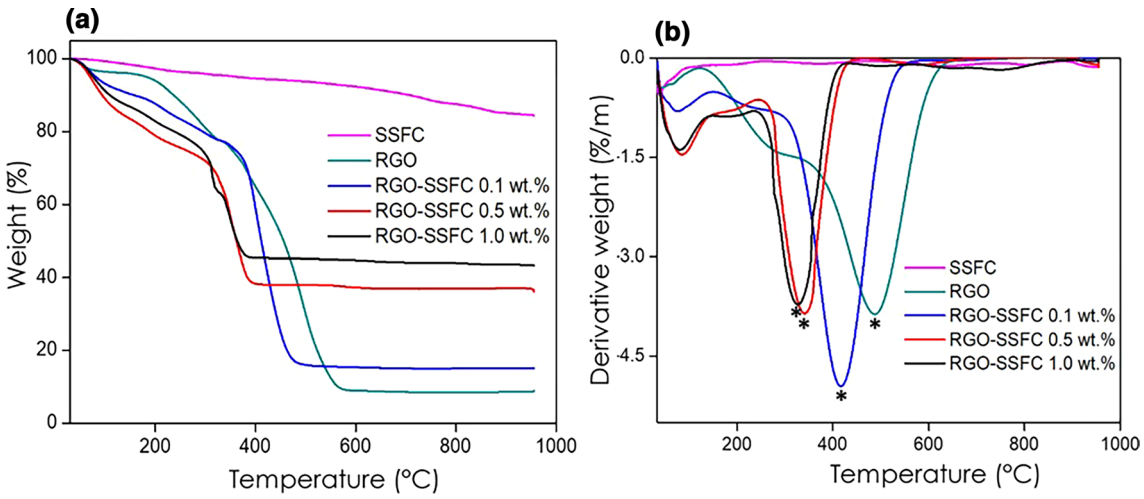

Fig. 7 Thermograms of (a) the prepared samples and (b) their first-derivative plots. * denotes exothermic peaks.

addition of SSFC, the nanocomposites became less thermally stable with decomposition temperatures of 410 °C, 390 °C, and 380 °C for RGO-SSFC-0.1, RGO-SSFC-0.5, and RGO-SSFC-1.0, respectively. Park et al.[63] reported a similar TGA thermogram of RGO. This was supported by Raman analysis (Fig. 5), which revealed that an increase in defect sites on the RGO lattice reduces the crystallinity as the I_D/I_G ratio increases upon adding more SSFC onto RGO. The residual amounts of RGO-SSFC-0.1, RGO-SSFC-0.5, and RGO-SSFC-1.0 were 16%, 38%, and 45%, respectively, which could be attributed to remnant SSFC that remains trapped inside the nanocomposites. Exothermic peaks, which indicate the exothermic reactions of graphene in air, were also observed.

Magnetic Properties

The magnetization (M_s) hysteresis loop taken at room temperature is shown in Supplementary Fig. S2. The hysteresis loops for SSFC are ferromagnetic (see Supplementary Fig. S2(a)), while GO and RGO-SSFC (see Supplementary Fig. S2(b) and (c)) are observed as paramagnetic. Different M_s parameters, such as saturation M_s, coercivity (H_c), and squareness (R), are given in Table III. These parameters mainly depend on the preparation technique, nanoparticle sizes, and the existence of cations. Both Fe and Co atoms are the primary sources for generating the magnetic moment from SSFC, which was found to have the highest M_s compared to RGO and RGO-SSFC. This could be linked to the ferromagnetic behavior, which has a canted internal spin and a large fraction of the uncompensated spin on the perovskite surface sample.[58,64] Generally, GO is an electrical insulator; however, its magnetization can be attributed to the Hubbard type.[65] The presence of different functional groups on the graphene skeleton can disrupt the sp^2-bonded hexagonal carbon sheet, and, in addition, can lead to isolated dangling bonds, which carry local moments that contribute to the paramagnetic moment nature of RGO and RGO-SSFC nanocomposites.

The variation of SSFC content in the RGO sheet was noted to change the magnetic properties of the nanocomposites. The M_s of the nanocomposites increased with R and decreased with H_c as the particle sizes decreased. The increase in M_s could be related to the formation of smaller particle sizes (see Sect. 3.2.1), which leads to lower surface distortion based on the interaction between the RGO sheet and transition metal ions (SSFC) on the spinel lattice of oxygen atoms.[66] Also, M_s was noted to increase with the content of SSFC on RGO, and this trend could be related to the super-exchange interaction on the oxygen vacancies based on the perovskite oxide that disturbs the antiparallel spin-ordering as Fe^{4+}-O^{2-}-Fe^{4+} and Fe^{3+}-O-Fe^{3+}.[67] In this case, an external field of the magnetic particle is proportional to the particle sizes.

Table III Magnetic parameters of SSFC, RGO and RGO-SSFC

Samples	Ms (emu/g) ± 0.1	H_c (Oe) ± 0.1	R ± 0.001
SSFC	37.4	144.3	0.273
RGO	1.3	27.6	0.003
RGO-SSFC-0.1	1.8	81.5	0.003
RGO-SSFC-0.5	2.0	50.4	0.006
RGO-SSFC-1.0	2.8	33.2	0.007

Optical Properties

UV–Vis Analysis

The UV–Vis absorption spectra used to investigate the optical absorption and band gap properties of SSFC, RGO, and RGO-SSFC are shown in Fig. 8. The SSFC samples in Fig. 8a strongly absorb between 240 nm and 300 nm in the UV region, and have an energy band gap of 3.8 eV, as shown in Fig. 8c. RGO and RGO-SSFC, in Fig. 8b, revealed an absorption band in the 239–335 nm and 271–400 nm wavelength ranges, respectively. This could be associated with the intrinsic band gap transition, which is associated with the $\pi - \pi^*$ transition based on the C-C aromatic bonds on the RGO sheet.[68] The presence of SSFC in the RGO-SSFC nanocomposites led to the appearance of small absorption bands between the wavelengths of 240 nm and 298 nm. The RGO and RGO-SSFC nanocomposites reveal small peaks at around 730 nm. A possible explanation could be that the photoluminescence emissions of molecules under UV–Vis irradiation may originate from a near-band-edge (NBE) emission level in the UV (or closer to the region), and as a result of deep-level defect emission often in a region beyond the first emission line (often in the visible region), possibly leading to observance of two emission peaks. The emission is a result of the recombination of the excited electrons at levels below or near the conduction band to the valence holes,[69] although, the emission intensity of the NBE emission and that of the deep-level emission varies. Generally, it is known that low emission (fluorescence) intensity indicates less charge recombination and high separation rates, which is often the intrinsic property sought in photoactive materials.[70] Furthermore, crystal defects could serve as a trap to enable electrons to capture one or more compositing materials or as a point source of recombination for charges, and this might increase the emission (fluorescence) intensity.[71,72] Note that a deep-level defect emission signifies the existence of intrinsic defects in the material nanostructures, which probably explains the second emission intensity at about 730 nm.

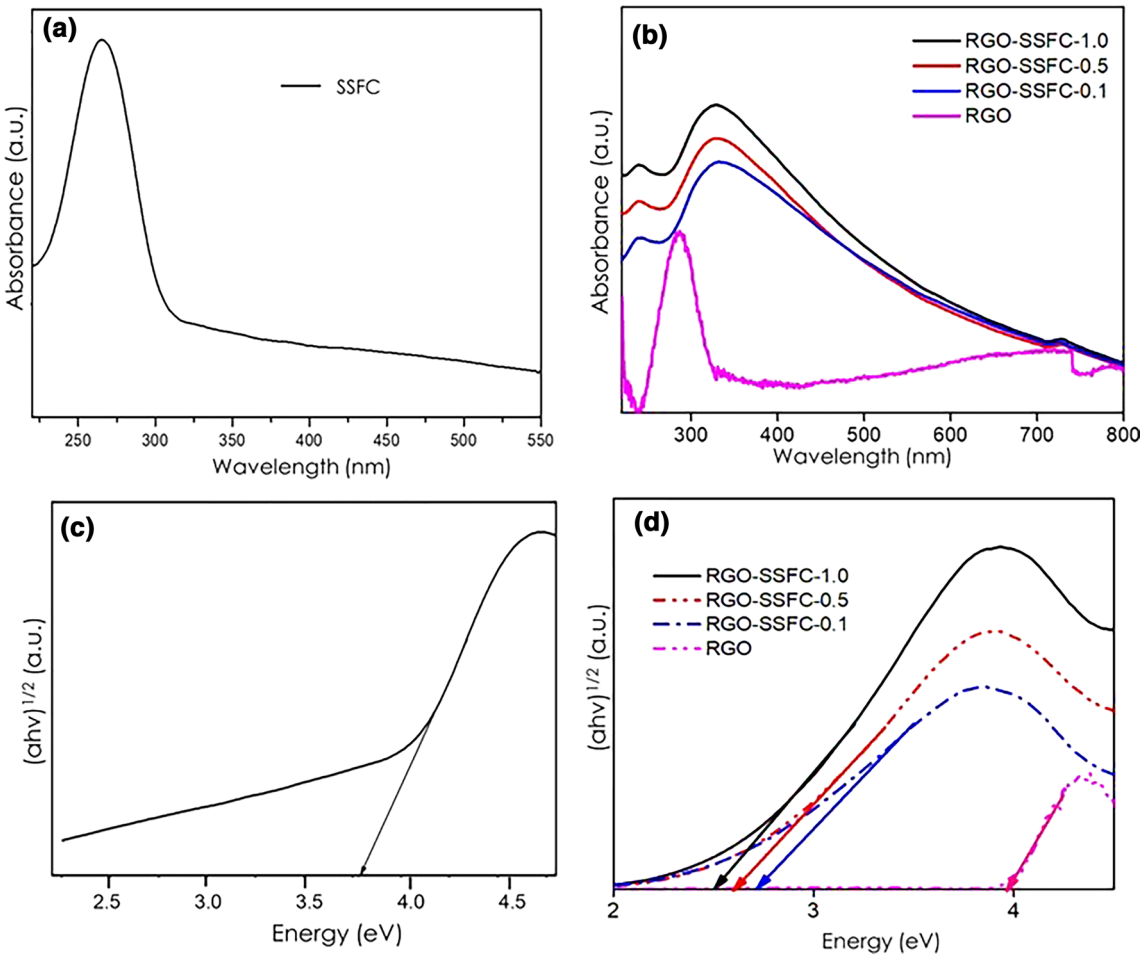

Fig. 8 UV–Vis (a) spectrum of SSFC and (b) spectra of RGO and RGO-SSFC nanocomposites. Energy band gap of (c) SSFC and (d) RGO and RGO-SSFC nanocomposites.

Thus, the fabrication of SSFC and RGO to form nanocomposites significantly reduced the energy band gaps compared to pristine RGO. There was a reduction of energy band gaps with more incorporation of SSFC nanoparticles, i.e., the band gaps of RGO, RGO-SSFC-0.1, RGO-SSFC-0.5, and RGO-SSFC-1.0 were determined to be 3.9 eV, 2.7 eV, 2.6 eV, and 2.4 eV, respectively, as shown in Fig. 8d. A similar trend was noted by Li et al.[40], where $BiFeO_3$ was combined with RGO, resulting in a reduction of the energy band gap relative to pristine RGO. The reduction in the energy band gap for RGO-SSFC would be beneficial for electron transportation in solar cells.

Electron–hole Transition

The charge recombination rate of various nanocomposites was investigated using the PL spectra, as shown in Fig. 9a and b. The PL spectra for SSFC, RGO, RGO-SSFC-0.1, RGO-SSFC-0.5, and RGO-SSFC-1.0 were obtained at an excitation wavelength of 300 nm. SSFC displayed a distinct peak in the 570–625 nm range with a maximum of 608 nm. RGO and RGO-SSFC exhibited distinct peaks in the range of 650–710 nm range, with a maximum of 682 nm. From the spectra in Fig. 9a, there is no spectral overlap and hence the variability in terms of intensities can only be observed in the RGO and RGO-SSFC nanocomposites as a result of the changes in the ratios of RGO-SSFC in Fig. 9b. SSFC was noted to have the highest intensity of about 735 a.u.; thus, it can lead to high charge recombination. On the other hand, RGO had a low intensity of about 83 a.u., indicating a low charge recombination rate. RGO sheets can absorb photons, generate excitons, and separate electrons and holes, but the issue with RGO is that it can immediately allow charges to recombine quickly, which results in RGO being combined with the SSFC elements (Sr, Sm, Co, and Fe).[73,74] The integration of RGO with SSFC was found to quench the PL, symbolizing a decrease in the charge recombination rate, allowing them to be better RGO-SSFC semiconductors[75]

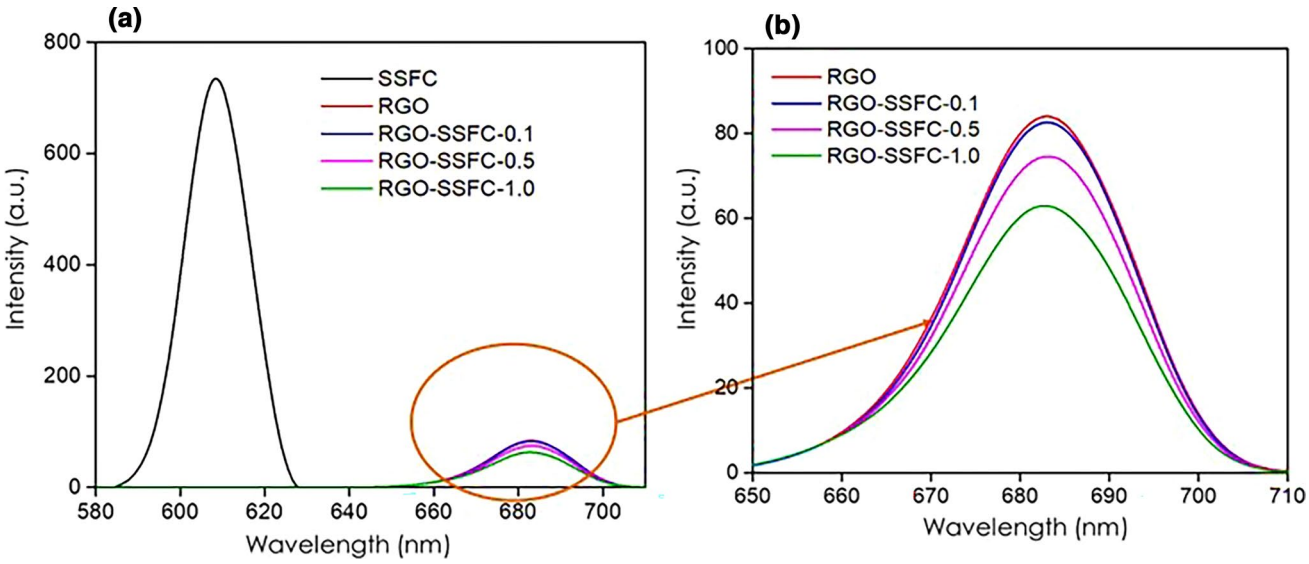

Fig. 9 Photoluminescence spectra of (a) SSFC and RGO-SSFC nanocomposites and (b) RGO-SSFC nanocomposites in a closer view.

Table IV Electrical conductivity parameters of SSFC, RGO and RGO-SSFC

Samples	Resistivity (Ω cm)	Conductivity (S cm^{-1})
SSFC	0.496	2.02
RGO	0.258	3.88
RGO-SSFC-0.1	0.162	6.17
RGO-SSFC-0.5	0.151	6.62
RGO-SSFC-1.0	0.159	6.29

Electrical Conductivity

The electrical conductivity characteristics and I–V curves of SSFC, RGO, RGO-SSFC-0.1, RGO-SSFC-0.5, and RGO-SSFC-1.0 are shown in Supplementary Fig. S3 and Table IV, respectively. SSFC exhibited a curved I–V slope, which was associated with its high electrical resistivity. On the other hand, RGO displayed a linear I–V slope, which was attributed to the high electrical conductivity of RGO due to the reduction in oxygenated functional groups. SSFC and RGO exhibited electrical conductivities of 2.02 S cm^{-1} and 3.88 S cm^{-1}, respectively. The addition of SSFC onto RGO sheets led to an improvement in electrical conductivity to 6.17 S cm^{-1}, 6.62 S cm^{-1} , and 6.29 S cm^{-1} for RGO-SSFC-0.1, RGO-SSFC-0.5, and RGO-SSFC-1.0, respectively. The improvement in electrical conductivity of RGO-SSFC nanocomposites compared to SSFC and RGO could be attributed to the strong synergistic interaction between the RGO sheets and SSFC elements (Sr, Sm, Co, and Fe), which allows for the easy transfer of charge carriers between the dye and the semiconductor material.

Electrochemical Properties

The CV of SSFC, RGO, and RGO-SSFC are shown in Fig. 10a–e, where all the prepared samples were obtained at the scan rate of 100 mV s^{-1} in the potential rate of − 0.6 V to 0.4 V. The CV curve of SSFC and RGO reveals Faradaic redox behavior. The presence of oxygen functional groups in SSFC would decrease the electrical conductivity, which can easily deteriorate in the aqueous electrolyte. Some distortion on the RGO can hinder the cation diffusion and charge collection on the electrode.[76] The CV curves for RGO-SSFC nanocomposites exhibited the electric double-layer capacitive behavior. The addition of SSFC onto RGO would enhance the electrochemical activity due to the introduction of SSFC, which creates defects on RGO on the electrode surface, thus resulting in the acceleration of charge transfer across the electrode. The addition of SSFC onto RGO to form the RGO-SSFC enhanced the electrical conductivity and wettability with a typical pseudo-capacitance material by lowering the charge transfer resistance, which can lead to excellent electrochemical performance, consequently improving the capacitance.[77] The prepared samples were further investigated using EIS.

Furthermore, the EIS of the prepared samples was investigated using Nyquist plots, as shown in Fig. 10f. The Nyquist plots of SSFC and RGO show the impedance behavior as a straight line in the low-frequency range and as a semicircle in the high-frequency range, indicating Faradaic reactions.[78] The EIS plot of the RGO-SSFC nanocomposites showed a

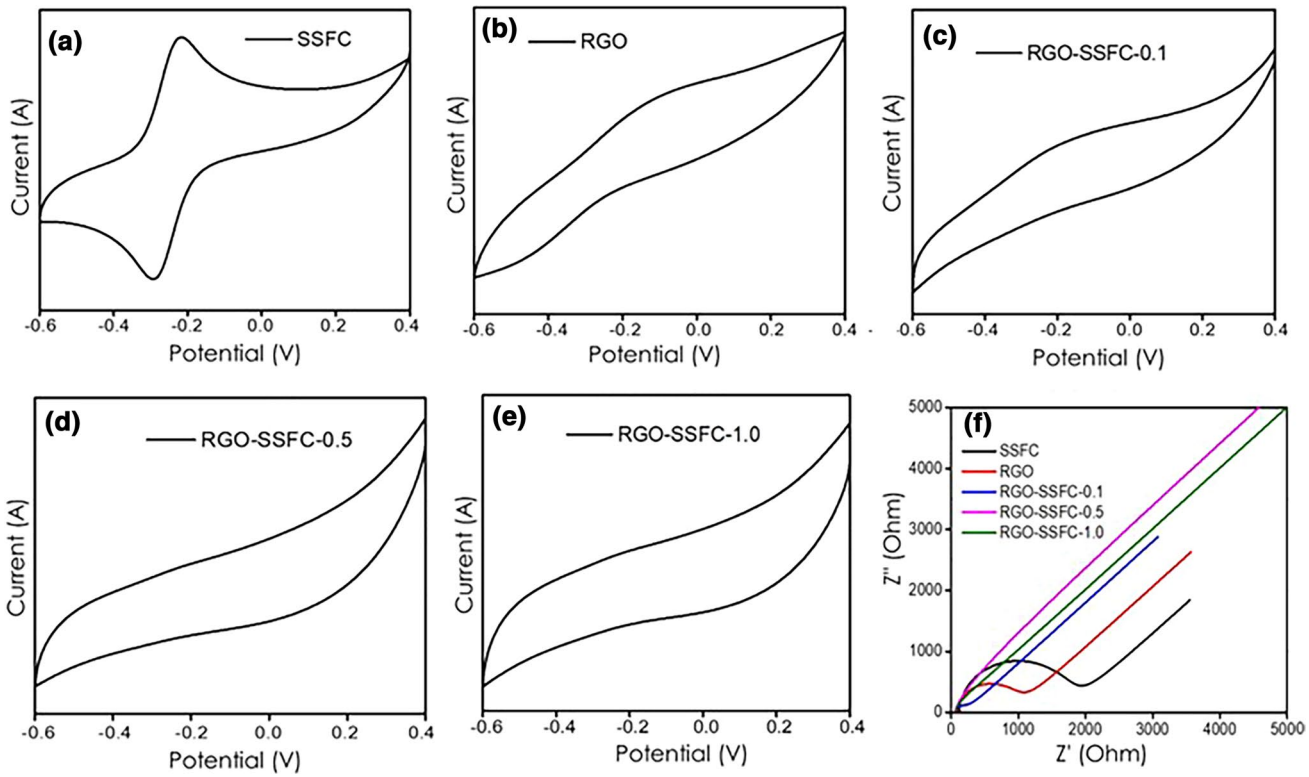

Fig. 10 Cyclic voltammograms of (a) SSFC, (b) RGO, (c) RGO-SSFC-0.1, (d) RGO-SSFC-0.5, (e) RGO-SSFC-1.0, and (f) Nyquist plots.

small semicircle compared to SSFC and RGO due to the low Faradaic reactions, which led to a small charge transfer resistance (R_{ct}) at the electrode–electrolyte interface, thus improving the electrical conductivity.[79] The R_{ct} was calculated from the EIS data. The R_{ct} of SSFC, RGO, RGO-SSFC-0.1, RGO-SSFC-0.5, and RGO-SSFC-1.0 are 178.2 Ω, 32.3 Ω, 23.7 Ω, and 26.1 Ω, respectively. Compared to the RGO-SSFC nanocomposites, the R_{ct} values for SSFC and RGO were relatively high due to superior interfacial resistance, which would slow the charge transfer within the electrode. This indicates that the addition of SSFC onto RGO allowed for the efficient separation of photogenerated charges (electron–hole pairs), which resulted in faster charge transfer and enhanced catalytic activities. As a result, RGO-SSFC-0.5 exhibited the lowest R_{ct} compared to the other nanocomposites due to its high surface area, which improved the contact between it and the electrolyte by exposing more active sites to increase the conductivity, whereas the pores in RGO-SSFC-0.5 would promote electrolyte diffusion to facilitate electron transfer.[80] Thus, RGO-SSFC-0.5 displayed the best electrochemical properties.

Application of RGO-SSFC Nanocomposites in DSSCs Devices

All the prepared samples were applied as semiconductor layers in DSSCs. The photovoltaic characteristics studied using a solar simulator are shown in Fig. 11. The PCE was calculated using[81]:

$$\mathrm{PCE} = \frac{V_{oc} J_{sc} \mathrm{FF}}{P_{in}} \tag{3}$$

where V_{oc} is the open-circuit voltage, J_{sc} is the short-circuit current, FF is the fill factor, and P_{in} is the incident light power.[82] Three experiments were prepared per device, and the best data were selected. The experimental data of various devices are presented in Table V. For comparison purposes, two dyes, i.e., Eosin B and MK-2, were used to investigate the effect of changing the light harvester (dye) on the photovoltaic parameters of DSSCs. Eosin B and MK-2 dyes were chosen based on their remarkable properties, such as easily tunable optoelectronic properties, high molar extinction coefficients, and enhanced environmental compatibility.[83,84] The performance of the DSSC was highly dependent on the amount of RGO-SSFC used. SSFC did not exhibit any V_{oc}, J_{sc}, FF, and PCE values on either device tested by Eosin or

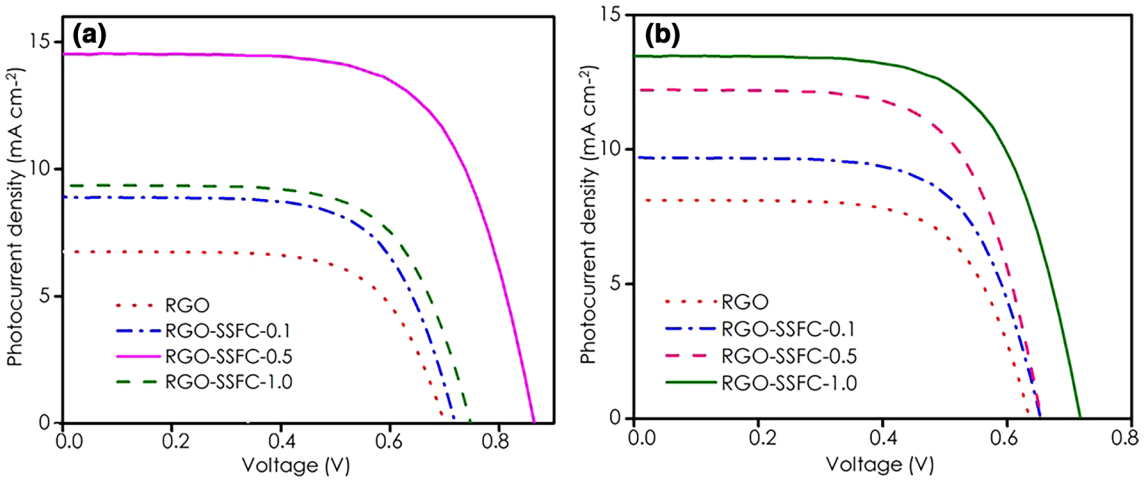

Fig. 11 *J–V* characteristics of various RGO-SSFC measured using (a) Eosin B and (b) MK-2.

Table V Photovoltaic parameters of RGO-SSFC tested using organic dyes as solar harvesters

Samples	Dye type	V_{oc} (V)	J_{sc} (mA cm^{-2})	FF (%)	PCE (%)
		± 0.01	± 0.20	± 2	± 0.10
RGO	Eosin-B	0.72	5.81	43	3.80
SSFC	Eosin-B	–	–	–	–
RGO-SSFC-0.1	Eosin-B	0.75	8.25	52	6.10
RGO-SSFC-0.5	Eosin-B	0.84	14.02	77	7.25
RGO-SSFC-1.0	Eosin-B	0.78	9.31	58	6.34
RGO	MK-2	0.62	8.17	51	3.98
SSFC	MK-2	–	–	–	–
RGO-SSFC-0.1	MK-2	0.64	9.73	53	6.42
RGO-SSFC-0.5	MK-2	0.64	12.90	60	6.97
RGO-SSFC-1.0	MK-2	0.74	13.15	59	7.01

MK-2 dyes. This could be due to the high energy band gap of 3.8 eV shown in Fig. 8, resulting from the poor band alignment, low electron mobility, and high recombination rate observed in Fig. 9, making it challenging to transfer electrons from the semiconductor to the collecting electrode.[85] The low PCE of RGO, when tested using both dyes, can be linked to the ultra-fast charge carrier recombination that normally occurs on the sheet and the poor light absorption when applied to the photoanode interface.[86]

As revealed earlier by Raman analysis, the introduction of SSFC nanoparticles onto RGO sheets created many defects in the RGO lattice, resulting in the formation of more active sites for better Eosin B or MK-2 dye adsorption. This, in turn, increased light absorption, and hence improved charge carrier photogeneration, resulting in relatively high J_{sc} , FF, and PCE. Also, an increase in J_{sc}, FF, and PCE can be attributed to the improvement in optical properties, such as the energy band gap level reduction from 3.8 eV to 2.5 eV for SSFC to RGO-SSFC, which would result in the reduction in charge recombination on RGO-SSFC, as shown in Fig. 9. So, the enhanced optical properties can improve electron transportation on the semiconductors once excited by the dye using a solar simulator. The low V_{oc} on RGO-SSFC-0.1 probably increased the photo-injected electrons recombination rate with Eosin B/MK-2 dye molecules due to poor band alignment between the dye and the semiconductor interface.[86] This trend was supported by the high charge recombination rate obtained in PL analysis, as shown in Fig. 9. RGO-SSFC-0.5 and RGO-SSFC-1.0 showed an increase in V_{oc} due to increased surface areas, which would enhance dye loading to harvest more light energy, as revealed in Table V. The enhanced surface area can result in more effective distribution of the dye molecules with less agglomeration on the semiconductor layer.

The relatively low FF could have mainly resulted from the leakage current, which arises from the agglomeration of the dye on the RGO-SSFC-0.1 semiconductor layer when using the MK-2 dye.[59] Also, the weak interaction of the electrolyte with the photoanode can lower the FF, which leads to a leakage current. On the other hand, the decrease in J_{sc} for the RGO-SSFC-0.1 and RGO-SSFC-0.5 devices prepared with MK-2 can be related to the poor electron transport and higher charge recombination rate between the RGO-SSFC semiconductor layer and the MK-2 dye molecules due to the agglomeration of the dye on the semiconductor layer.[87] Lee et al.[86] noted a similar finding. The Eosin B dye-based DSSCs outperformed their MK-2-based counterparts, of which the RGO-SSFC-0.5-based DSSCs with the Eosin B

dye exhibited the highest J_{sc}, and hence the highest PCE of 7.25%. This was attributed to the larger surface area of RGO-SSFC-0.5 and excellent electrical conductivity, which facilitated the effective adsorption and loading of dye molecules, as well as the efficient transfer of electrons, resulting in enhanced efficiency. Also, since the electron injection rate greatly depends on the conduction band of the RGO-SSFC and lowest unoccupied molecular orbital level of the harvester, a perfect match of these two can enhance electron transfer and suppress charge carrier recombination, thereby improving device performance.

Conclusions

RGO-SSFC nanocomposites were successfully synthesized using a hydrothermal technique. SEM images revealed the RGO sheet to be densely decorated by irregular- and spherically-shaped SSFC nanoparticles. XRD revealed the formation of primary phase structures in the RGO-SSFC samples, which lowered the crystalline nature of the nanocomposites. The addition of SSFC onto the RGO sheet promoted the formation of defects or disorders on the RGO sheet. FTIR confirmed the formation of different functional groups due to the synergistic interaction between SSFC and RGO. Adding SSFC of smaller particle sizes onto RGO increased the surface area. The addition of SSFC onto the RGO sheet also improved the optical properties of the nanocomposites, as well as reduced the charge recombination rate. The magnetic hysteresis of SSFC and RGO-SSFC were ferromagnetic and paramagnetic, respectively. The increase in M_s of the RGO-SSFC nanocomposites was affected by the formation of smaller particle sizes and the improvement in the surface area. Using cheaper and greener organic dyes, such as Eosin B and MK-2, on the RGO-SSFC semiconductors can improve their environmental compatibility and reduce the cost and environmental impact of DSSCs. Our findings demonstrate that RGO-SSFC-0.5 loaded with Eosin B is a potential photoanode material for DSSCs, suitable for further investigation and for optimizing device performance.

Supplementary Information The online version contains supplementary material available at https://doi.org/10.1007/s11664-023-10526-3.

Acknowledgments The authors express gratitude to the University of KwaZulu-Natal (UKZN); National Research Foundation (NRF) under Grant numbers 107740, 103979, 145770 and 121165; Moses Kotane Institution, UKZN Nanotechnology Platform and Eskom Tertiary Education Support Programme (TESP) for their support and funding of this research.

Author contributions Conceptualisation: SN, EM, MAO and VON; methodology: SN, EM, MAO and VON; software: SN, EM, MAO and VON; validation: SN, EM, MAO and VON; formal analysis: SN, EM, MAO and VON; investigation: SN, EM, MAO and VON; resources: VON; data curation: SN, EM and VON; writing-original draft preparation: SN, EM, MAO and VON; writing-review and editing: SN; visualisation: SN, EM and VON; supervision: VON; project administration: VON; funding acquisition: VON.

Conflict of interest The authors declare no conflict of interest.

References

1. R. Schlesinger, F. Bianchi, S. Blumstengel, C. Christodoulou, R. Ovsyannikov, B. Kobin, K. Moudgil, S. Barlow, S. Hecht, and S. Marder, Efficient light emission from inorganic and organic semiconductor hybrid structures by energy-level tuning. *Nat. Commun.* 6, 6754 (2015). https://doi.org/10.1038/ncomms7754.
2. Z. Zhou, Z. Qiang, T. Sakamaki, I. Takei, R. Shang, and E. Nakamura, Organic/Inorganic hybrid p-type semiconductor doping affords hole-transporting-layer-free thin-film perovskite solar cells with high stability. *ACS appl. Mater. Interfaces.* 11, 22603 (2019). https://doi.org/10.1021/acsami.9b06513.
3. Y.H. Lee, M. Ha, I. Song, J.H. Lee, Y. Won, S. Lim, H. Ko, and J.H. Oh, High-performance hybrid photovoltaics with efficient interfacial contacts between vertically aligned ZnO nanowire arrays and organic semiconductors. *ACS Omega* 4, 9996 (2019). https://doi.org/10.1021/acsomega.9b00778.
4. D. Devadiga, M. Selvakumar, P. Shetty, and M. Santosh, Dye-sensitized solar cell for indoor applications: a mini-review. *J. Electron. Mater.* 50, 3187 (2021). https://doi.org/10.1007/s11664-021-08854-3.
5. Y. Lu, Q. Liu, J. Luo, B. Wang, T. Feng, X. Zhou, X. Liu, and Y. Xie, Solar cells sensitized with porphyrin dyes containing oligo (ethylene glycol) units: a high efficiency beyond 12%. *Chemsuschem* 12, 2802 (2019). https://doi.org/10.1002/cssc.201900139.
6. C.-P. Lee, C.-T. Li, and K.-C. Ho, Use of organic materials in dye-sensitized solar cells. *Mater. Today.* 20, 267 (2017). https://doi.org/10.1016/j.mattod.2017.01.012.
7. B. Lee, J. He, R.P. Chang, and M.G. Kanatzidis, All-solid-state dye-sensitized solar cells with high efficiency. *Nature* 485, 486 (2012). https://doi.org/10.1038/nature11067.
8. Y. Cui, W. Wang, N. Li, R. Ding, and K. Hong, Hetero-seed meditated method to synthesize ZnO/TiO_2 multipod nanostructures with ultra-high yield for dye-sensitized solar cells. *J. Alloys Compd.* 805, 868 (2019). https://doi.org/10.1016/j.jallcom.2019.07.169.
9. J.V. Krishna, G. Reddy, K. Devulapally, N. Islavath, and L. Giribabu, Solution processed aligned ZnO nanowires as anti-reflection and electron transport layer in organic dye-sensitized solar cells. *Opt. Mater.* 95, 109243 (2019). https://doi.org/10.1016/j.optmat.2019.109243.
10. X. Du, W. Li, L. Zhao, X. He, H. Chen, and W. Fang, Electron transport improvement in CdSe-quantum dot solar cells using ZnO nanowires in nanoporous TiO_2 formed by foam template.

J. Photochem. Photobiol. A. 371, 144 (2019). https://doi.org/10.1016/j.jphotochem.2018.10.054.
11. H. Zhu, J. Wei, K. Wang, and D. Wu, Applications of carbon materials in photovoltaic solar cells. *Sol. Energy Mater Sol. Cells.* 93, 1461 (2009). https://doi.org/10.1016/j.solmat.2009.04.006.
12. P. Charoeythornkhajhornchai, K. Tedsree, and R. Chancharoen, Effect of carbazole coating on TiO_2 nanoparticles as a photosensitizer and MWCNTs on the performance of epoxy composites. *J. Sci. Adv. Mater. Dev.* 6, 425 (2021). https://doi.org/10.1016/j.jsamd.2021.05.001.
13. G. Williams, B. Seger, and P.V. Kamat, TiO_2-graphene nanocomposites. UV-assisted photocatalytic reduction of graphene oxide. *ACS Nano* 2, 1487 (2008). https://doi.org/10.1021/nn800251f.
14. A.R. Jeyaraman, S.K. Balasingam, C. Lee, H. Lee, B. Balakrishnan, S. Manickam, M. Yi, H.-J. Kim, K.S. Nallathambi, and Y. Jun, Enhanced solar to electrical energy conversion of titania nanoparticles and nanotubes-based combined photoanodes for dye-sensitized solar cells. *Mater. Lett.* 243, 180 (2019). https://doi.org/10.1016/j.matlet.2019.02.006.
15. S. Barja, M. Garnica, J.J. Hinarejos, A.L.V. de Parga, N. Martín, and R. Miranda, Self-organization of electron acceptor molecules on graphene. *ChemComm.* 46, 8198 (2010). https://doi.org/10.1039/C0CC02675A.
16. K.I. Bolotin, K. Sikes, Z. Jiang, M. Klima, G. Fudenberg, J. Hone, P. Kim, and H. Stormer, Ultrahigh electron mobility in suspended graphene. *Solid State Commun.* 146, 351 (2008). https://doi.org/10.1016/j.ssc.2008.02.024.
17. A.B. Monnappa, J.G.G. Manjunatha, A.S. Bhatt, and H. Nagarajappa, Sensitive and selective electrochemical detection of vanillin at graphene based poly (methyl orange) modified paste electrode. *J. Sci. Adv. Mater. Dev.* 6, 415 (2021). https://doi.org/10.1016/j.jsamd.2021.05.002.
18. C. Lee, X. Wei, J.W. Kysar, and J. Hone, Measurement of the elastic properties and intrinsic strength of monolayer graphene. *Science* 321, 385 (2008). https://doi.org/10.1126/science.1157996.
19. A.A. Balandin, S. Ghosh, W. Bao, I. Calizo, D. Teweldebrhan, F. Miao, and C.N. Lau, Superior thermal conductivity of single-layer graphene. *Nano Lett.* 8, 902 (2008). https://doi.org/10.1021/nl073187 2.
20. R.R. Nair, P. Blake, A.N. Grigorenko, K.S. Novoselov, T.J. Booth, T. Stauber, N.M. Peres, and A.K. Geim, Fine structure constant defines visual transparency of graphene. *Science* 320, 1308 (2008). https://doi.org/10.1126/science.1156965.
21. J. Tian, L. Guo, X. Yin, and W. Wu, The liquid-phase preparation of graphene by shear exfoliation with graphite oxide as a dispersant. *Mater. Chem. Phys.* 223, 1 (2019). https://doi.org/10.1016/j.matchemphys.2018.10.039.
22. D.-J. Hsu, Y.-W. Chi, K.-P. Huang, and C.-C. Hu, Electrochemical activation of vertically grown graphene nanowalls synthesized by plasma-enhanced chemical vapor deposition for high-voltage supercapacitors. *Electrochim. Acta.* 300, 324 (2019). https://doi.org/10.1016/j.electacta.2019.01.134.
23. Z. Sun, Z. Yan, J. Yao, E. Beitler, Y. Zhu, and J.M. Tour, Growth of graphene from solid carbon sources. *Nature* 468, 549 (2010). https://doi.org/10.1038/nature09579.
24. C. Wang, T. Jiang, K. Zhao, A. Deng, and J. Li, A novel electrochemiluminescent immunoassay for diclofenac using conductive polymer functionalized graphene oxide as labels and gold nanorods as signal enhancers. *Talanta* 193, 184 (2019). https://doi.org/10.1016/j.talanta.2018.09.103.
25. G. Ruan, Z. Sun, Z. Peng, and J.M. Tour, Growth of graphene from food, insects, and waste. *ACS Nano* 5, 7601 (2011). https://doi.org/10.1021/nn202625c.
26. H. Aguilar-Bolados, A. Contreras-Cid, A. Neira-Carrillo, M. Lopez-Manchado, and M. Yazdani-Pedram, Removal of surfactant from nanocomposites films based on thermally reduced graphene oxide and natural rubber. *J. Compos. Sci.* 3, 31 (2019). https://doi.org/10.3390/jcs3020031.
27. W. Gao, L.B. Alemany, L. Ci, and P.M. Ajayan, New insights into the structure and reduction of graphite oxide. *Nat. Chem.* 1, 403 (2009). https://doi.org/10.1038/nchem.281.
28. E. Singh and H.S. Nalwa, Graphene-based bulk-heterojunction solar cells: a review. *J. Nanosci. Nanotechnol.* 15, 6237 (2015). https://doi.org/10.1166/jnn.2015.11654.
29. C. Botas, P. Álvarez, P. Blanco, M. Granda, C. Blanco, R. Santamaría, L.J. Romasanta, R. Verdejo, M.A. López-Manchado, and R. Menéndez, Graphene materials with different structures prepared from the same graphite by the Hummers and Brodie methods. *Carbon* 65, 156 (2013). https://doi.org/10.1016/j.carbon.2013.08.009.
30. K. Chakraborty, S. Chakrabarty, T. Pal, and S. Ghosh, Synergistic effect of zinc selenide–reduced graphene oxide towards enhanced solar light-responsive photocurrent generation and photocatalytic 4-nitrophenol degradation. *New J. Chem.* 41, 4662 (2017). https://doi.org/10.1039/C6NJ04022E.
31. S.P. Jiang, Development of lanthanum strontium cobalt ferrite perovskite electrodes of solid oxide fuel cells–a review. *Int. J. Hydrog. Energy.* 44, 7448 (2019). https://doi.org/10.1016/j.ijhydene.2019.01.212.
32. J. Zhou, P. Li, X. Zhang, J. Yan, and X. Qi, Effect of configurational entropy on dielectric properties of high-entropy perovskite oxides $(Ce_{0.5}, K_{0.5})x[(Bi_{0.5}, Na_{0.5})_{0.25}Ba_{0.25}Sr_{0.25}Ca_{0.25}]_{1-x}TiO_3$. *J. Mater. Sci. Mater. Electron.* (2022). https://doi.org/10.1007/s10854-022-08882-7.
33. M.S. Sheikh, A.P. Sakhya, R. Maity, A. Dutta, and T. Sinha, Narrow band gap and optical anisotropy in double perovskite oxide Sm_2NiMnO_6: a new promising solar cell absorber. *Sol. Energy Mater Sol. Cells.* 193, 206 (2019). https://doi.org/10.1016/j.solmat.2019.01.015.
34. Y. Wei, J. Liu, Z. Zhao, A. Duan, G. Jiang, C. Xu, J. Gao, H. He, and X. Wang, Three-dimensionally ordered macroporous $Ce_{0.8}Zr_{0.2}O_2$-supported gold nanoparticles: synthesis with controllable size and super-catalytic performance for soot oxidation. *Energy Environ. Sci.* 4, 2959 (2011). https://doi.org/10.1039/C0EE00813C.
35. C. Aydin, H. Aydin, M. Taskin, and F. Yakuphanoglu, A novel study: the effect of graphene oxide on the morphology, crystal structure, optical and electrical properties of lanthanum ferrite based nano electroceramics synthesized by hydrothermal method. *J. Nanosci. Nanotechnol.* 19, 2547 (2019). https://doi.org/10.1166/jnn.2019.15841.
36. C.B. Njoku and R.J. Kriek, Application of $Sm_{0.8}Sr_{0.2}Fe_{1-x}Co_xO_{3-\delta}$ (x= 0.2, 0.5, 0.8) perovskite for the oxygen evolution reaction in alkaline media. *Electrocatalysis* 10, 305 (2018). https://doi.org/10.1007/s12678-018-0498-7.
37. Y. Yang, H. Fei, G. Ruan, L. Li, G. Wang, N.D. Kim, and J.M. Tour, Carbon-free electrocatalyst for oxygen reduction and oxygen evolution reactions. *ACS Appl. Mater. Interfaces.* 7, 20607 (2015). https://doi.org/10.1021/acsami.5b04887.
38. C.C. Wang, Y. Cheng, E. Ianni, S.P. Jiang, and B. Lin, A highly active and stable $La_{0.5}Sr_{0.5}Ni_{0.4}Fe_{0.6}O_{3-\delta}$ perovskite electrocatalyst for oxygen evolution reaction in alkaline media. *Electrochim. Acta.* 246, 997 (2017). https://doi.org/10.1016/j.electacta.2017.06.161.
39. X.B. Xie, J. Xiao, Q. Xu, M. Chen, D.C. Chen, D.P. Huang, and F. Zhang, Property evaluation of $Sm_{1-x}Sr_xFe_{0.7}Cr_{0.3}O_{3-\delta}$ perovskites as cathodes for intermediate temperature solid oxide fuel cells. *Int. J. Energy Res.* 43, 2832 (2019). https://doi.org/10.1002/er.4377.
40. T. Li, J. Shen, N. Li, and M. Ye, Hydrothermal preparation, characterization and enhanced properties of reduced graphene-$BiFeO_3$

nanocomposite. *Mater. Lett.* 91, 42 (2013). https://doi.org/10.1016/j.matlet.2012.09.045.
41. W.S. Hummers Jr. and R.E. Offeman, Preparation of graphitic oxide. *J. Am. Chem. Soc.* 80, 1339 (1958). https://doi.org/10.1021/ja01539a017.
42. E.T. Mombeshora, R. Simoyi, V.O. Nyamori, and P.G. Ndungu, Multiwalled carbon nanotube-titania nanocomposites: understanding nano-structural parameters and functionality in dye-sensitized solar cells. *S. Afri. J. Chem.* 68, 153 (2015). https://doi.org/10.17159/0379-4350/2015/v68a22.
43. I.-K. Ding, J. Melas-Kyriazi, N.-L. Cevey-Ha, K.G. Chittibabu, S.M. Zakeeruddin, M. Grätzel, and M.D. McGehee, Deposition of hole-transport materials in solid-state dye-sensitized solar cells by doctor-blading. *Org. Electron.* 11, 1217 (2010). https://doi.org/10.1016/j.orgel.2010.04.019.
44. H. Gerischer, Charge transfer processes at semiconductor-electrolyte interfaces in connection with problems of catalysis. *Surf. Sci.* 18, 97 (1969). https://doi.org/10.1016/0039-6028(69)90269-6.
45. C. Fu, G. Zhao, H. Zhang, and S. Li, Evaluation and characterization of reduced graphene oxide nanosheets as anode materials for lithium-ion batteries. *Int. J. Electrochem. Sci.* 8, 6269 (2013).
46. D. Selvakumar, H. Sivaram, A. Alsalme, A. Alghamdi, and R. Jayavel, Freestanding flexible, pure and composite form of reduced graphene oxide paper for ammonia vapor sensing. *Sci. Rep.* 9, 8749 (2019). https://doi.org/10.1038/s41598-019-45408-4.
47. C.J. Bartel, C. Sutton, B.R. Goldsmith, R. Ouyang, C.B. Musgrave, L.M. Ghiringhelli, and M. Scheffler, New tolerance factor to predict the stability of perovskite oxides and halides. *Sci. Adv.* 5, 0693 (2019). https://doi.org/10.1126/sciadv.aav0693.
48. N. Li, M. Zheng, X. Chang, G. Ji, H. Lu, L. Xue, L. Pan, and J. Cao, Preparation of magnetic $CoFe_2O_4$-functionalized graphene sheets via a facile hydrothermal method and their adsorption properties. *J. Solid State Chem.* 184, 953 (2011). https://doi.org/10.1016/j.jssc.2011.01.014.
49. J. Hu, L. Wang, L. Shi, and H. Huang, Preparation of $La_{1-x}Ca_xMnO_3$ perovskite–graphene composites as oxygen reduction reaction electrocatalyst in alkaline medium. *J. Power Sources.* 269, 144 (2014). https://doi.org/10.1016/j.jpowsour.2014.07.004.
50. W. Li, H. Dong, X. Guo, N. Li, J. Li, G. Niu, and L. Wang, Graphene oxide as dual functional interface modifier for improving wettability and retarding recombination in hybrid perovskite solar cells. *J. Mater. Chem. A.* 2, 20105 (2014). https://doi.org/10.1039/C4TA05196C.
51. M. Acik and S.B. Darling, Graphene in perovskite solar cells: device design, characterization and implementation. *J. Mater. Chem. A.* 4, 6185 (2016). https://doi.org/10.1039/C5TA09911K.
52. M.N. Sithole, B. Omondi, and P.G. Ndungu, Synthesis and characterization of $Ce_{0.6}Sr_{0.4}Fe_{0.8}Co_{0.2}O_{3-\delta}$ perovskite material: potential cathode material for low temperature SOFCs. *J. Rare Earths.* 35, 389 (2017). https://doi.org/10.1016/S1002-0721(17)60924-4.
53. H. Lu, F. Liang, Y. Yao, J. Gou, and D. Hui, Self-assembled multilayered carbon nanofiber nanopaper for significantly improving electrical actuation of shape memory polymer nanocomposite. *Compos. B. Eng.* 59, 191 (2014). https://doi.org/10.1016/j.compositesb.2013.12.009.
54. Y. Ye, P. Wang, E. Dai, J. Liu, Z. Tian, C. Liang, and G. Shao, A novel reduction approach to fabricate quantum-sized SnO_2-conjugated reduced graphene oxide nanocomposites as non-enzymatic glucose sensors. *Phys. Chem. Chem. Phys.* 16, 8801 (2014). https://doi.org/10.1039/C4CP00554F.
55. G. Wang, X. Sun, F. Lu, Q. Yu, C. Liu, and J. Lian, Controlled synthesis of MnSn $(OH)_6$/graphene nanocomposites and their electrochemical properties as capacitive materials. *J. Solid State Chem.* 185, 172 (2012). https://doi.org/10.1016/j.jssc.2011.11.015.
56. X. Fan, J. Guan, X. Cao, W. Wang, and F. Mou, Low-temperature synthesis, magnetic and microwave electromagnetic properties of substoichiometric spinel cobalt ferrite octahedra. *Eur. J. Inorg. Chem.* 2010, 419 (2010). https://doi.org/10.1002/ejic.200900681.
57. J. Li, Y. Wang, H. Ling, Y. Qiu, J. Lou, X. Hou, S.P. Bag, J. Wang, H. Wu, and G. Chai, Significant enhancement of the visible light photocatalytic properties in 3D $BiFeO_3$/graphene composites. *Nanomaterials* 9, 65 (2019). https://doi.org/10.3390/nano9010065.
58. S. Phokha, S. Pinitsoontorn, S. Maensiri, and S. Rujirawat, Structure, optical and magnetic properties of $LaFeO_3$ nanoparticles prepared by polymerized complex method. *J. Solgel Sci Technol.* 71, 333 (2014). https://doi.org/10.1007/s10971-014-3383-8.
59. K. Kakiage, Y. Aoyama, T. Yano, K. Oya, J.-I. Fujisawa, and M. Hanaya, Highly-efficient dye-sensitized solar cells with collaborative sensitization by silyl-anchor and carboxy-anchor dyes. *Chem-Comm.* 51, 15894 (2015). https://doi.org/10.1039/C5CC06759F.
60. N.P. Ngidi, E. Muchuweni, and V.O. Nyamori, Synthesis and characterisation of heteroatom-doped reduced graphene oxide/bismuth oxide nanocomposites and their application as photoanodes in DSSCs. *RSC Adv.* 12, 2462 (2022). https://doi.org/10.1039/D1RA08888B.
61. K.S. Sing, Reporting physisorption data for gas/solid systems with special reference to the determination of surface area and porosity (Recommendations 1984). *Pure Appl. Chem.* 57, 603 (1985). https://doi.org/10.1351/pac198557040603.
62. A. Lerf, H. He, M. Forster, and J. Klinowski, Structure of graphite oxide revisited. *J. Phys. Chem. B.* 102, 4477 (1998). https://doi.org/10.1021/jp9731821.
63. O.-K. Park, Y.-M. Choi, J.Y. Hwang, C.-M. Yang, T.-W. Kim, N.-H. You, H.Y. Koo, J.H. Lee, B.-C. Ku, and M. Goh, Defect healing of reduced graphene oxide via intramolecular cross-dehydrogenative coupling. *Nanotechnology* 24, 185604 (2013). https://doi.org/10.1088/0957-4484/24/18/185604.
64. A.P. Amaliya, S. Anand, and S. Pauline, Investigation on structural, electrical and magnetic properties of titanium substituted cobalt ferrite nanocrystallites. *J. Magn. Magn. Mater.* 467, 14 (2018). https://doi.org/10.1016/j.jmmm.2018.07.058.
65. K. Bagani, A. Bhattacharya, J. Kaur, A. Rai Chowdhury, B. Ghosh, M. Sardar, and S. Banerjee, Anomalous behaviour of magnetic coercivity in graphene oxide and reduced graphene oxide. *J. Appl. Phys.* 115, 023902 (2014). https://doi.org/10.1063/1.4861173.
66. N.D. Mohallem and L.M. Seara, Magnetic nanocomposite thin films of $NiFe_2O_4/SiO_2$ prepared by sol–gel process. *Appl. Surf. Sci.* 214, 143 (2003). https://doi.org/10.1016/S0169-4332(03)00304-0.
67. C. Sasikala, G. Suresh, N. Durairaj, I. Baskaran, B. Sathyaseelan, E. Manikandan, R. Srinivasan, and M.K. Moodley, Chemical, morphological, structural, optical and magnetic properties of transition metal titanium (Ti)-doped $LaFeO_3$ nanoparticles. *J. Supercond. Nov. Magn.* 32, 1791 (2019). https://doi.org/10.1007/s10948-018-4879-1.
68. X. Gao, Y. Shang, L. Liu, and W. Nie, A plasmonic Z-scheme three-component photocatalyst g-C_3N_4/Ag/$LaFeO_3$ with enhanced visible-light photocatalytic activities. *Opt. Mater.* 88, 229 (2019). https://doi.org/10.1016/j.optmat.2018.11.030.
69. S. Tonda, S. Kumar, S. Kandula, and V. Shanker, Fe-doped and-mediated graphitic carbon nitride nanosheets for enhanced photocatalytic performance under natural sunlight. *J. Mater. Chem. A.* 2, 6772 (2014). https://doi.org/10.1039/C3TA15358D.
70. M.S. Amer, P. Arunachalam, A.M. Al-Mayouf, S. Prasad, M.N. Alshalwi, and M.A. Ghanem, Mesoporous tungsten trioxide photoanodes modified with nitrogen-doped carbon quantum dots for

enhanced oxygen evolution photo-reaction. *Nanomaterials* 9, 1502 (2019). https://doi.org/10.3390/nano9101502.
71. S. Yousaf, T. Kousar, M.B. Taj, P.O. Agboola, I. Shakir, and M.F. Warsi, Synthesis and characterization of double heterojunction-graphene nano-hybrids for photocatalytic applications. *Ceram. Int.* 45, 17806 (2019). https://doi.org/10.1016/j.ceramint.2019.05.352.
72. J.-Y. Liu, Y. Bai, P.-Y. Luo, and P.-Q. Wang, One-pot synthesis of graphene–BiOBr nanosheets composite for enhanced photocatalytic generation of reactive oxygen species. *Catal. Commun.* 42, 58 (2013). https://doi.org/10.1016/j.catcom.2013.07.043.
73. A. Kongkanand, R. Martínez Domínguez, and P.V. Kamat, Single wall carbon nanotube scaffolds for photoelectrochemical solar cells. Capture and transport of photogenerated electrons. *Nano Lett.* 7, 676 (2007). https://doi.org/10.1021/nl0627238.
74. M. Grätzel, Conversion of sunlight to electric power by nanocrystalline dye-sensitized solar cells. *J. Photochem. Photobiol. A.* 164, 3 (2004). https://doi.org/10.1016/j.jphotochem.2004.02.023.
75. Y. Yu, C.Y. Jimmy, C.-Y. Chan, Y.-K. Che, J.-C. Zhao, L. Ding, W.-K. Ge, and P.-K. Wong, Enhancement of adsorption and photocatalytic activity of TiO_2 by using carbon nanotubes for the treatment of azo dye. *Appl. Catal. B: Environ.* 61, 1 (2005). https://doi.org/10.1016/j.apcatb.2005.03.008.
76. Z. Li, Y. Mi, X. Liu, S. Liu, S. Yang, and J. Wang, Flexible graphene/MnO_2 composite papers for supercapacitor electrodes. *J. Mater. Chem.* 21, 14706 (2011). https://doi.org/10.1039/C1JM11941A.
77. Y. Li, X. Xu, Y. He, Y. Jiang, and K. Lin, Nitrogen doped macroporous carbon as electrode materials for high capacity of supercapacitor. *Polymers* 9, 2 (2017). https://doi.org/10.3390/polym9010002.
78. C. Peng, L. Yanyue, J. Yuanyuan, W. Haiyan, and L. Zijiong, Synthesis of $LaMnO_3$-reduced graphene oxide or Sr composite and their application in electrochemical properties. *Mater. Res. Express.* 7, 025023 (2020). https://doi.org/10.1088/2053-1591/ab715c.
79. C.I. Priyadharsini, G. Marimuthu, T. Pazhanivel, P. Anbarasan, V. Aroulmoji, S. Prabhu, and R. Ramesh, Electrochemical supercapacitor studies of Ni^{2+}-doped $SrTiO_3$ nanoparticles by a ball milling method. *Ionics* 26, 3591 (2020). https://doi.org/10.1007/s11581-019-03412-8.
80. H. Zou, B. He, P. Kuang, J. Yu, and K. Fan, Ni_xS_y nanowalls/nitrogen-doped graphene foam is an efficient trifunctional catalyst for unassisted artificial photosynthesis. *Adv. Funct. Mater.* 28, 1706917 (2018). https://doi.org/10.1002/adfm.201706917.
81. M. Grätzel, Dye-sensitized solar cells. *J. Photochem. Photobiol. C.* 4, 145 (2003). https://doi.org/10.1016/S1389-5567(03)00026-1.
82. R.D. Costa, F. Lodermeyer, R. Casillas, and D.M. Guldi, Recent advances in multifunctional nanocarbons used in dye-sensitized solar cells. *Energy Environ. Sci.* 7, 1281 (2014). https://doi.org/10.1039/C3EE43458C.
83. P. Ferdowsi, Y. Saygili, F. Jazaeri, T. Edvinsson, J. Mokhtari, S.M. Zakeeruddin, Y. Liu, M. Grätzel, and A. Hagfeldt, Molecular engineering of simple metal-free organic dyes derived from triphenylamine for dye-sensitized solar cell applications. *Chemsuschem* 13, 212 (2020). https://doi.org/10.1002/cssc.201902245.
84. T. Raguram and K. Rajni, Effects of varying the soaking duration of Eosin Blue sensitized TiO_2 photoanodes for dye-sensitized solar cells. *Optik. Inpress* 204, 164169 (2020). https://doi.org/10.1016/j.ijleo.2020.164169.
85. I. Abdulkadir, S.B. Jonnalagadda, and B.S. Martincigh, Synthesis and effect of annealing temperature on the structural, magnetic and photocatalytic properties of $(La_{0.5}Bi_{0.2}Ba_{0.2}Mn_{0.1})FeO_{(3-\delta)}$. *Mater. Chem. Phys.* 178, 196 (2016). https://doi.org/10.1016/j.matchemphys.2016.05.007.
86. J.E. Benedetti, A.D. Gonçalves, A.L. Formiga, M.-A. De Paoli, X. Li, J.R. Durrant, and A.F. Nogueira, A polymer gel electrolyte composed of a poly (ethylene oxide) copolymer and the influence of its composition on the dynamics and performance of dye-sensitized solar cells. *J. Power Sources.* 195, 1246 (2010). https://doi.org/10.1016/j.jpowsour.2009.09.008.
87. A. de Morais, L.M. Loiola, J.E. Benedetti, A.S. Gonçalves, C.A. Avellaneda, J.H. Clerici, M.A. Cotta, and A.F. Nogueira, Enhancing in the performance of dye-sensitized solar cells by the incorporation of functionalized multi-walled carbon nanotubes into TiO_2 films: the role of MWCNT addition. *J. Photochem. Photobiol. A.* 251, 78 (2013). https://doi.org/10.1016/j.jphotochem.2012.09.016.

Authors and Affiliations

Samantha Ndlovu[1] · Edigar Muchuweni[2] · Moses A. Ollengo[1] · Vincent O. Nyamori[1]

✉ Vincent O. Nyamori
nyamori@ukzn.ac.za

Samantha Ndlovu
samanthandlovu36@gmail.com

Edigar Muchuweni
emuchuweni@buse.ac.zw

Moses A. Ollengo
mosesollengo@gmail.com

[1] School of Chemistry and Physics, University of KwaZulu-Natal, Westville Campus, Private Bag X54001, Durban 4000, South Africa

[2] Department of Engineering and Physics, Bindura University of Science Education, Private Bag 1020, Bindura, Zimbabwe